MAPPING SUBGLACIAL GEOMORPHOLOGY AND STRUCTURE IN A COLLISIONAL OROGEN: AN EXAMPLE FROM THE MALASPINA GLACIER, ALASKA

by

Michelle Marie Cotton

A thesis submitted to the faculty of
The University of Utah
in partial fulfillment of the requirements for the degree of

Master of Science

in

Geology

Department of Geology and Geophysics

The University of Utah

December 2011

The University of Utah Graduate School

STATEMENT OF THESIS APPROVAL

The thesis of **Michelle Marie Cotton**

has been approved by the following supervisory committee members:

Ronald Bruhn	, Chair	**9/19/2011** Date Approved
Richard Forster	, Member	**9/28/2011** Date Approved
David Chapman	, Member	**10/31/11** Date Approved

and by **D. Kip Solomon** , Chair of

the Department of **Geology and Geophysics**

and by Charles A. Wight, Dean of The Graduate School.

ABSTRACT

The Malaspina Glacier of Southern Alaska /Yukon Canada provides the opportunity to investigate the interaction between glaciers and tectonics, in an active orogen that is forming from the collision and accretion of the Yakutat Microplate in the Gulf of Alaska. Several large alpine glaciers coalesce on the piedmont of the Saint Elias Mountains to form the Malaspina Glacier. We use feature tracking by cross correlation of Landsat satellite images to map the velocity and strain rate fields on the surface of the Malaspina Glacier to explore how the structural geology at the bed of the glacier affects the dynamics and structure of the moving ice on the surface. Rates of flow in alpine areas are fast and ice can move 90+ m/month in the summer and on the piedmont ice can move over 100-300 m a year. Strain rates calculated from the velocity fields are on the order of 10^-9 / s on the surface of the glaciers. Strain rate maps reveal the nature of the stress field in the ice where it moves over topographic features at the bed of the glacier. The results bear directly on the origin of ice falls that originate at thrust faults on the limbs of large folds, the origin of fast glacier flow along fault zones where rheology at the bed of the glacier is presumably impacted by rapid erosion and development of weak water saturated till, the pattern of ice flow around the termination of a large strike slip fault, and the presence and extent of subglacial lakes and distributary channels that feed outburst flooding at the terminus of glaciers. The morphology and dynamics of the Malaspina piedmont lobes also provide insight into the strike slip component of motion

along the Esker Creek Fault that was activated during an M 8.1 earthquake in 1899, as well as some control on the basal topography, and perhaps structural geology, where the Fairweather Transform Fault and Aleutian Megathrust are currently linking together beneath the Malaspina Glacier.

TABLE OF CONTENTS

ABSTRACT……...iii

ACKNOWLEDGEMENTS……..vii

INTRODUCTION……...1

GEOLOGIC BACKGROUND..……10

Regional Tectonics ……10
Geology of Study Area ……12
Stratigraphic Cover……13
Major Geologic Structures……14

THE MALASPINA GLACIER SYSTEM……....17

Glacial Dynamics……...17
Glacial Surface Features……18
Glacial Topography……....19

METHODS……23

Image Acquisition and Preprocessing....……....23
Optical Feature Tracking ……...24
Strain Rate ……28
Glacier Analog Modeling ……..29

RESULTS ……32

Glacier Modeling...……33
Upper Seward Glacier……33
Lower Seward Glacier……...34
Agassiz Glacier……..38
The Seward Lobe……...40
Oily Lake....……...41

DISCUSION……71

Affects of Rock Structure on Ice Flow……..71

Interpretation of Flow Patterns……76
COSI-CORR- Relevance to Glacial Monitoring……80
General Observations on Glacier Structure and Hydrology……83

CONCLUSIONS……91

REFERENCES……95

ACKNOWLEDGEMENTS

First and foremost, I would like to thank my advisor, Dr. Ronald Bruhn, for his unending guidance and support; he has been a source of wisdom and inspiration over the past two years. I would also like to thank my committee members, Dr. Richard Forester and Dr. David Chapman, for their guidance and input into my research. A great thanks to NASA and Jeanne Sauber for funding my research as well as being a wonderful resource for ideas and knowledge. Thank you to my fellow graduate students who helped motivate me when I needed it most. Thank you to my Mom for her love and encouragement through the whole processes. Finally, thank you to my friends and family for all your help and support.

INTRODUCTION

The Saint Elias Mountains, in southern Alaska and Yukon, Canada, are located in an active orogen characterized by complex structural boundaries and extreme climatic influences that have formed the largest glaciers in North America (Fig. 1) (Plafker, 1987). The mountain peaks, rising to nearly 6 km, are blanketed with ice fields that spill out of the mountain fronts to feed two of the largest piedmont glaciers in North America, the Bering and Malaspina (Sharp, 1951). The majority of structural boundaries in the area are concealed beneath the ice with glaciers flowing along or across the major faults, providing the opportunity to study how tectonic and glacial processes interact to transform the landscape (Meigs and Sauber, 2000; Sauber et al., 2000; Spotilia et al., 2004).

The Malaspina Glacier System is situated in a regional structural transition from strike slip faulting along the Fairweather Fault to thrust faulting along the Aleutian Megathrust, making the topography of the region an example of the interplay between tectonics and erosion (Plafker, 1987; Bruhn et al., 2004). The Malaspina glacier is composed of three lobes, the central lobe being fed by the Seward Glacier, the western lobe being fed by the Agassiz Glacier, and the eastern lobe fed by the Marvine Glacier (Fig. 2) (Sharp, 1951). Underlying the glacier are several faults that accommodate the transition from strike slip to thrust faulting; most notable are the Fairweather Transform Fault, the Malaspina Fault, and the Esker Creek Fault (Figs. 3 and 4). The region is

currently undergoing deformation as recorded by geodetic measurements and seismicity (Fletcher and Freymueller, 1999; Elliott et al., 2010). Noteworthy earthquakes of the region are the two M8+ events of 1899 (Tarr and Martin, 1912; Shennan et al., 2009), the M 7.9 earthquake on the Fairweather Fault in 1958 and the M 7.1 Saint Elias earthquake, with associated aftershocks sourced beneath the Malaspina piedmont, in 1979 (Estabrook et al., 1992).

This study aims to use ice surface velocity patterns to infer the nature of basal topography and tectonic structures that lie beneath the glacier. Several examples are presented of how the topography, velocity field, and structure of the glacier ice changes where it flows over folds and faults that extend beneath the ice from where they are exposed in the adjacent mountains. These examples are compared with theoretical models and physical laboratory experiments concerning the perturbation of ice flow over basal topography and are also used to help identify geological structures where they are totally buried beneath the glacier. In this thesis, the problem of buried structures beneath the Malaspina Glacier is explored because of their significance to tectonic models and seismic potential of the Saint Elias Orogen. As comprehensive data on glacier flow is difficult to record in the field, velocity patterns on the ice will be derived from feature tracking pairs of Landsat satellite images.

Glacier dammed and subglacial lakes can also alter ice flow patterns, as the storage of water can dramatically impact glacier dynamics (Capps et al., 2010). The ability to identify the presence of glacial lakes and to map the course of water discharge beneath a glacier is important when investigating hazards posed by outburst floods, and also has the potential to advance our understanding of the mechanics of glacial surging.

Hence, we will also focus on how the presence of subglacial lakes affects glacier surface velocity and structure.

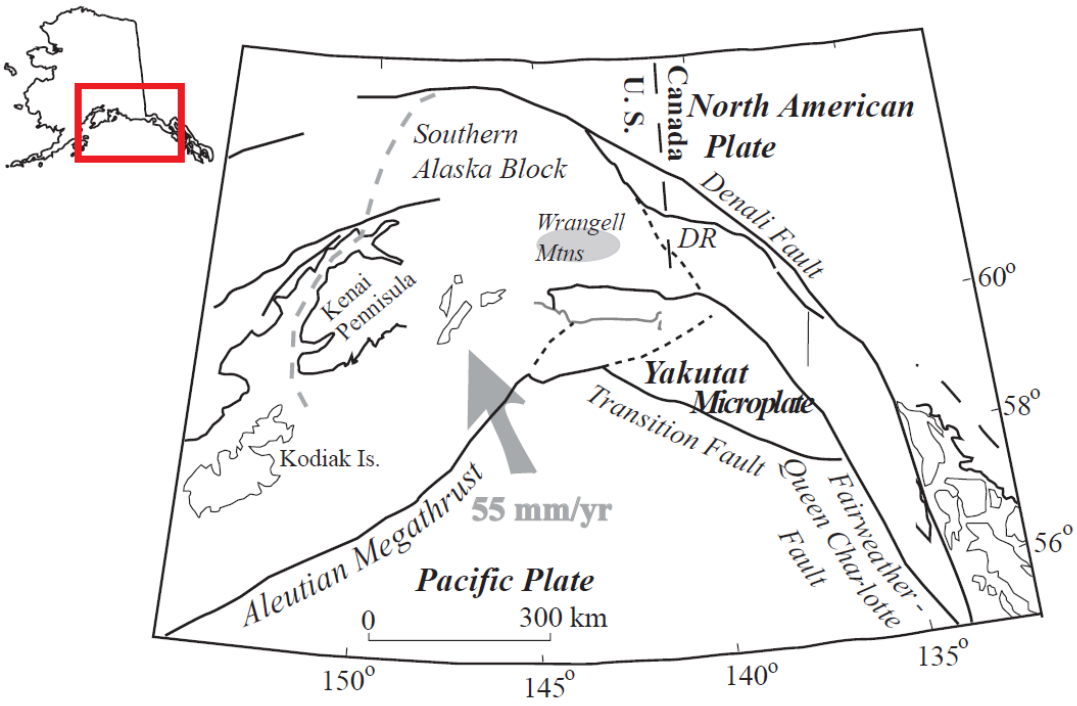

Figure 1. Tectonic elements of southern Alaska, illustrating the major faults and location of the Yakutat microplate. Relative plate movement between the Pacific and North American plates is 55 mm/yr aligned parallel to the large grey arrow. Figure modified from Bruhn et al., 2004.

,.

Figure 2. Composite Landsat Thematic Mapper image (bands 4, 3, 2) of the Malaspina Glacier System with subdivisions of the glacier highlighted within the red boxes A through E. Box A corresponds to the Upper Seward Glacier, box B corresponds to the Lower Seward Glacier, box C corresponds to the Seward Lobe, box D corresponds to the upper portion of the Agassiz Glacier, box E corresponds to the central portion of the Agassiz Glacier, box F corresponds to the Agassiz Lobe, and box G corresponds to the location of the Marvine lobe (not analyzed in this study but highlighted for reference location). The location of Oily Lake is highlighted in blue.

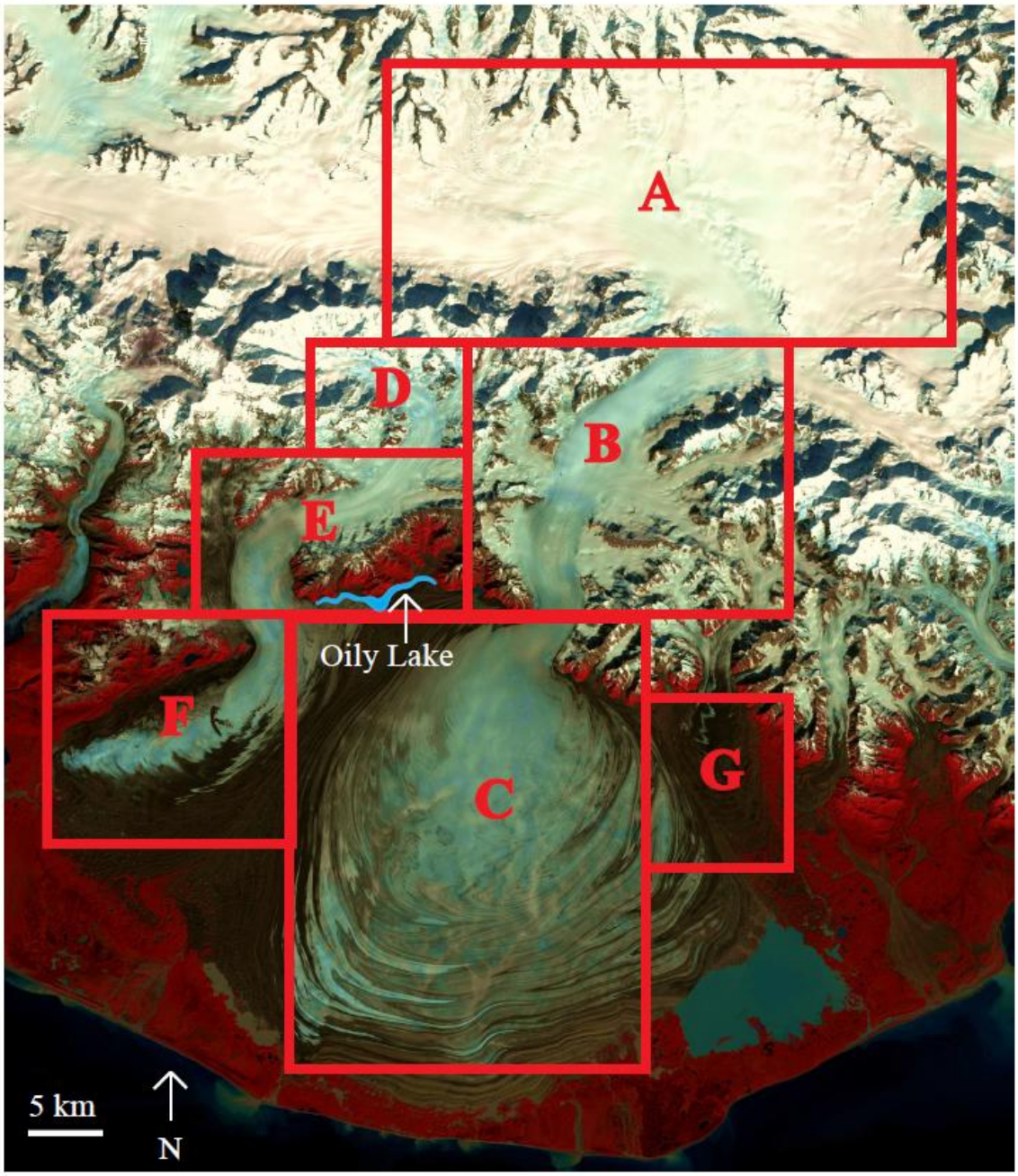
A
B
C
D
E
F
G
Oily Lake
5 km
N

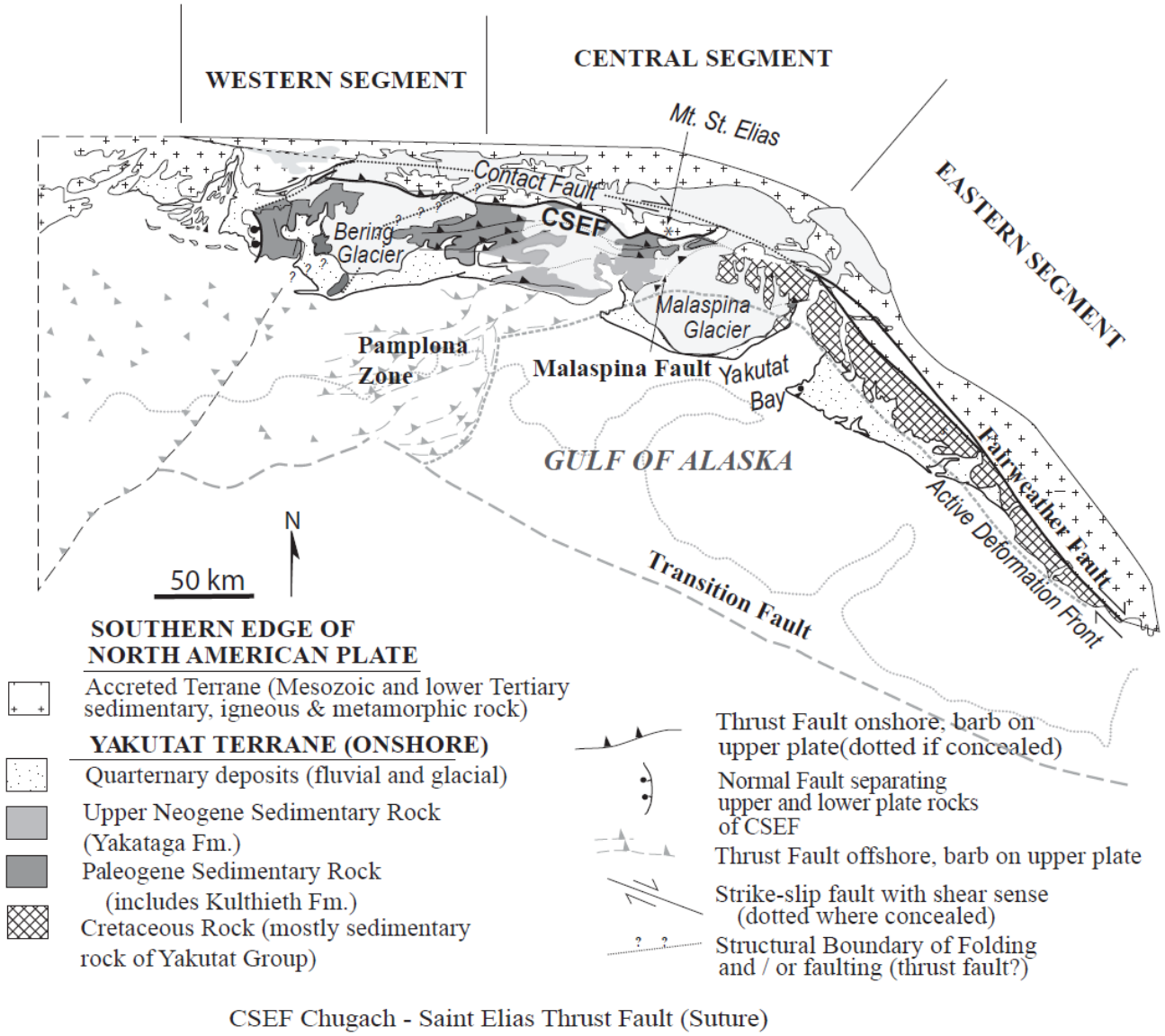

Figure 3. Regional geology and general stratigraphy of the Saint Elias orogen. The Malaspina glacier resides in a transitional region between the eastern and central segments. Refer to Figure 1 for the location of plate boundaries. Figure modified from Bruhn et al., 2004.

Figure 4. A geologic and stratigraphic map of the study area. Geologic cross section A-A' shown in Fig. 30 and B-B' shown in Fig.31. Figure modified from Richter et al. (2006).

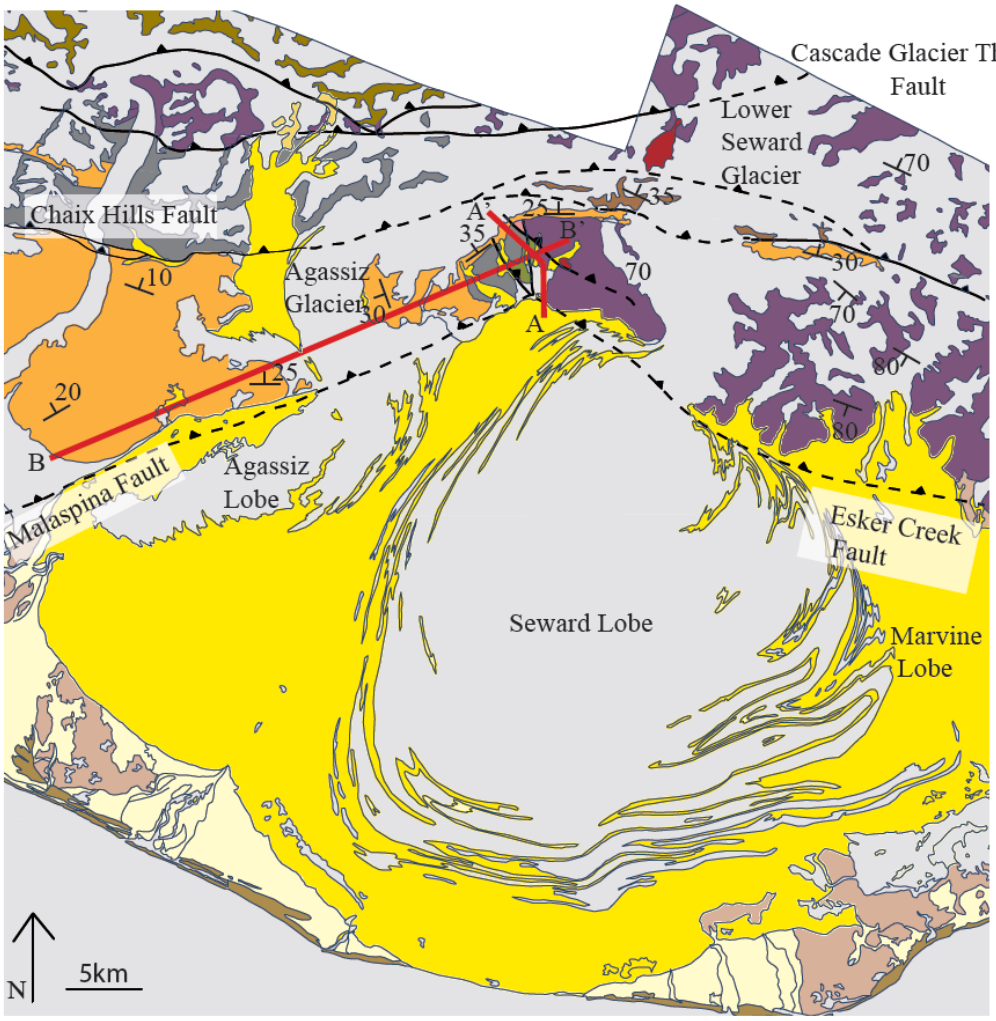

Modern river allivum

Morianes or glacial till

Landslide deposits

Yakataga Formation *(sandstones, siltstone, & conglomerates)*

Kultieth Formation (*sandstone, coal, & shale*)

Poul Creek Formation (*siltstone, claystone, sandstone, & conglomerate*)

Oily Lake Siltstone (*siltstone*)

Yakutat Group (*metmorphosed flysch and granite, gneiss and schist*)

Hubbs Creek Volcanics (*basalt*)

Chugach Terrane (*metamorphic terrane*)

Thrust fault, barbs on upper plate

Cross section line

GEOLOGIC BACKGROUND

Regional Tectonics

The St. Elias Mountains of southern Alaska and Yukon, Canada are part of an active orogen formed by the collision of the Yakutat microplate with the North American plate (Fig. 1). The Yakutat microplate originated from the coast of southeast Alaska and British Columbia during the early Tertiary and was transported northward along the transform fault boundary of the dextral Queen Charlotte/Fairweather transform fault system (Fig.1) (Plafker et al., 1978; Bruns, 1983; Plafker et al., 1994a; Bruhn et al., 2004). During the mid-to-late Miocene the Yakutat microplate began colliding with southern Alaska where it encountered the Aleutian Megathrust and became partially subducted beneath and accreted onto the continent (Plafker et al., 1994b). The subducted material is inferred to be oceanic lithosphere, possibly an oceanic plateau with unusually thick crust (Plafker et al., 1994b; Christeson et al., 2010). Flat slab subduction of the buoyant oceanic crust is responsible for the regional topography (Pavlis et al., 2004), deformation that extends far into interior Alaska, and formation of the Wrangell Mountain Volcanoes (Fig.1) (Page et al., 1989). The microplate is also driving orogenesis in the Fairweather, Saint Elias, and Chugach mountain ranges, where some of the world's greatest earthquakes and large tsunamis are generated (Bruhn et al., 2004; Shennan et al., 2009).

The Yakutat microplate contains a basaltic basement that is approximately 24-27

km thick that presumably originated as an oceanic plateau (Christeson et al., 2010), this is overlain by Cretaceous metamorphosed flysch and accretionary mélange formed from late Mesozoic subduction along the edge of the North America plate (Plafker, 1987; Bruhn et al., 2004). Overlying the basement rocks is sedimentary cover composed of approximately 4 km of Paleogene shallow marine and fluvial deposits followed by an angular unconformity above which lie sedimentary deposits that record the onset of glaciation and mountain building in the late Miocene (Plafker, 1987; Eyles et al. 1991; Plafker et al., 1994b). The Cretaceous basement is decoupled from underlying oceanic basement, with the oceanic crust being subducted beneath southern Alaska and the overlying Cretaceous and younger rocks becoming folded and faulted onshore as they accrete onto the continental margin (Fig. 3). The Yakutat microplate is colliding obliquely with southern Alaska at a rate of 45-55 mm/yr (Fletcher and Freymueller, 1999; Elliot et al., 2010). The oblique convergence is accommodated by a combination of dextral strike slip and thrust faulting and has formed three structural regions within the orogen, referred to as the eastern, central, and western segments of the Saint Elias Orogen (Fig. 3) (Bruhn et al., 2004). The eastern segment is bounded by the Fairweather Fault and contains a coastal mountain belt with associated transpressive structures (Fig. 3) (Bruhn et al., 2004; Chapman et al., 2008). The central segment's eastern boundary is the Pamplona Zone offshore and the Malaspina Fault onshore; this region contains the Chugach Saint Elias Fault which is the suture zone of the Yakutat microplate, and a belt of east-west trending foreland folds and thrusts (Fig. 3). The western segment is characterized by secondary deformation and refolding of older folds and thrust faults as well as the Chugach Saint

Elias fault in the region west of the Bering Glacier (Fig. 3) (Bruhn et al., 2004; Pavlis et al., 2004).

Geology of Study Area

This study focuses primarily on the transition between the eastern and central segments of the orogen (Figs. 3 and 4).This transition is structurally significant as it is situated in a orogenic corner or "syntaxis" where faulting styles change from dextral transform motion in the east along the Fairweather Fault to thrusting in the west along the Malaspina Fault. The Malaspina Glacier System overlies this tectonic corner covering the structures involved within the transition. Understanding how these structures link up beneath the ice is important as the faults are active and have the potential to generate great to large magnitude earthquakes.

Both the Pamplona Zone and Malaspina Fault are located within a region of spatially concentrated and intense seismicity (Doser et al., 2000). Offshore the Pamplona zone is a region of deformed Yakutat microplate that consists of a series of steeply dipping high angle thrust faults that sole into lower angle thrust faults at a depth of 2-8 km along the easternmost part of the Aleutian Megathrust (Fig. 3)(Worthington et al., 2010). The Pamplona zone has generated several large earthquakes including an M 6.1 earthquake in 1958 and M 6.7 to M 6.2 earthquakes in 1970 (Doser et al., 1997). The Malaspina Fault extends northward from the Pamplona Zone beneath the Agassiz Lobe of the Malaspina Glacier (Fig. 3) (Plafker et al., 1994a; Bruhn et al., 2004). Its location is constrained by well data from the Chaix Hills #1A exploration well, drilled by Standard Oil in 1961 (Plafker et al., 1975), earthquake relocations (Estabrook et al., 1992), tilting of foreland structures in the Samovar Hills (Bruhn et al., 2004), and evidence of fault

rupture in the M 8.1 earthquakes of 1899 (Shennan et al., 2009). The Malaspina and Pamplona Fault system is one of the youngest structures of the orogen and reflects the eastward propagation of the Aleutian Megathrust system during the Pliocene (Plafker, 1987; Estabrook et al., 1992; Shennan et al., 2009).

The structural syntaxis formed by the Fairweather and Malaspina Faults corresponds to the area of the greatest exhumation rate and highest topography in the orogen. Zircon fission track ages on detritus sourced from the Seward Glacier Basin are < 3Myr, indicating that the region is undergoing rapid uplift and erosion. The young ages and rapid uplift are unique to the Seward Glacier System and are not found in other parts of the orogen (Enkelmann et al., 2009). Rapid uplift is also evident by the mountain peaks that obtain elevations in excess of 5000 m where they rim the Seward Glacier Basin. Notable peaks include Mount Logan, the highest peak in Canada at 5959 m, Mount Vancouver (4812 m), and Mt. Saint Elias (5489 m).

Stratigraphic Cover

The main stratigraphic units (Fig. 5),within the study area are the Yakutat Group (Cretaceous to early Tertiary), Kulthieth Formation (Paleocene to early Eocene), Poul Creek Formation (latest Eocene to early Miocene), and the Yakataga Formation (late Miocene to present) (Plafker, 1987). Two minor stratigraphic units are present locally within the Samovar Hills, the Hubbs Creek Volcanics (Eocene 40-50 Ma) composed of Basalt and the Oily Lake Siltstone (Eocene 48-51 Ma)(Plafker et al. 1994b).

The Yakutat Group is several kilometers thick and composed of complexly deformed flysch and mélange. The flysch consists of greywacke, siltstone, and argillite, while the mélange contains discrete blocks of greenstone, limestone, marble, greywacke,

chert, conglomerate, and plutonic rocks in a sheared matrix of mudstone that is locally recrystallized to a green schist (Plafker, 1987). Structures and metamorphic isograds within the Yakutat Group are oriented northwest roughly parallel with the Fairweather fault. The Kulthieth Formation is a 2-3 km thick unit of arkosic sandstone, shales, and coal beds. The unit was deposited in a shallow marine deltaic environment (Plakfer, 1987). Within the Samovar Hills, the Kulthieth Formation consists of a 1-3 m thick white tuffaceous conglomerate which transitions upwards into 500 m of coarse sandstone and coal beds (Chapman et al., in press). The 1-2 km thick Poul Creek Formation is composed of concretionary marine siltstone, claystone, sandstone, conglomerate, minor basaltic tuff, and is locally glauconitic (Richter et al., 2006). The unit was deposited in marine waters adjacent to low lying coastal mountains, in a depositional environment marked by low sedimentation rates (Eyles et al., 1991). The Yakataga formation is a 0-6 km thick unit composed of the youngest rocks in the orogen consisting mainly of interbedded glaciomarine sandstone, mudstone, and diamictite deposited on the continental shelf (Plafker et al., 1978; Eyles and Lagoe, 1990). Deposition of the Yakataga Formation coincided with the onset of renewed mountain building along the coast of the Gulf of Alaska, and the onset of widespread global cooling and glaciation (Plafker, 1987; Eyles et al. 1991; Plafker et al., 1994b).

Major Geologic Structures

The major faults in the study area that are buried by ice and include the Fairweather Fault, a dextral transform fault that ends abruptly beneath the Upper Seward Glacier (Fig. 3); the Cascade Glacier Thrust Fault, a north dipping approximately east-west trending thrust fault that terminates near the fault tip of the Fairweather Fault in the

Upper Seward Glacier (Fig. 4); the Chaix Hills Fault, a thrust fault that dips north and strikes approximately east-west. The fault extends beneath the Agassiz Glacier and continues towards the east where it crosses beneath the Lower Seward Glacier and forms a structural duplex with the Dome Pass Fault (Fig. 4). The Dome Pass Fault is an east-west trending north dipping thrust fault (Fig. 4). The Malaspina fault, a thrust fault that dips towards the west, lies under the Agassiz Lobe of the Malaspina Glacier, and intersects with the Esker Creek Fault at roughly a 45 degree angle forming a tectonic groin in the southern front of the Samovar Hills (Fig. 4). The Esker Creek Fault is modeled as a north dipping thrust fault that connects to the Fairweather Fault in the east (Plafker and Thatcher, 2008).

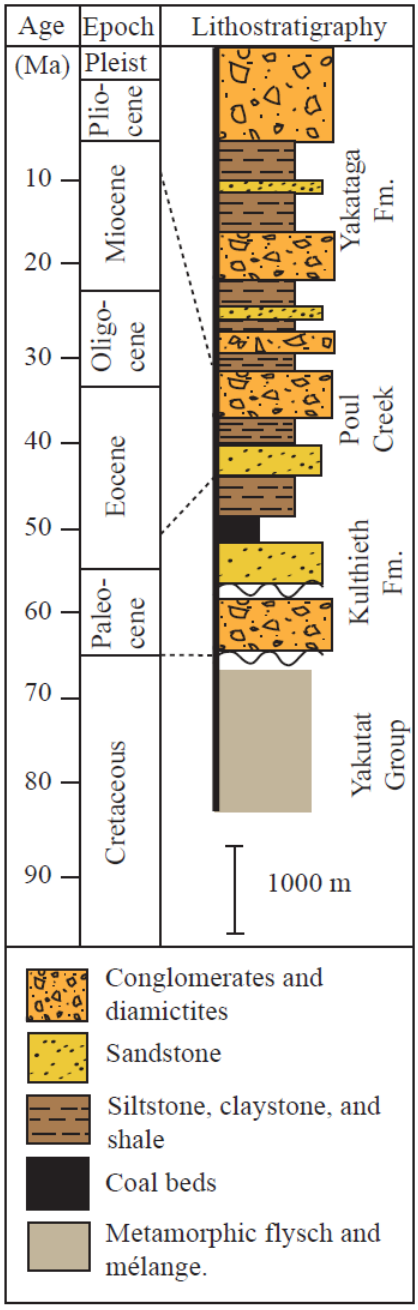

Figure 5. A general stratigraphic section for the study area. Figure modified from T.L. Pavlis in press 2011.

THE MALASPINA GLACIER SYSTEM

The Malaspina Glacier system is subdivided into several glaciers or lobes (Fig. 2). The Seward glacier (composed of the Upper Seward, Lower Seward, and Seward Lobe) is the largest central portion of the Malaspina glacier (Fig. 2A-C), followed by the Agassiz Glacier (composed of the upper, central, and Agassiz Lobe) in the west (Fig. 2D-F), and the Marvine glacier located in the east (Fig. 2G). Ice accumulates in the upper elevations of the Saint Elias Mountains and the ablation zone consists of the entire piedmont (Molnia, 2001; Muskett et al., 2008). The Marvine Glacier is not analyzed in this study but the Seward and Agassiz Glacier are discussed in detail.

Glacial Dynamics

The Malaspina Glacier System covers an area of approximately 5000 km^2 (Molnia, 2001), and occupies a large topographic basin on the piedmont that extends at least 320 m below sea level (Sharp, 1951; Molnia and Jones, 1989). Ice thickness on the piedmont ranges between 500 to 700 m (Conway et al., 2009). In the last 30 years, ice thinning has been observed and large elevation decreases in the ablation areas are correlated with increased temperatures in Yakutat and Cordova during 1976 to 2000, relative to the interval 1950 to 1975 (Muskett et al., 2003). From 1972/73 to 1999/2002 the surface of the Malaspina Glacier lowered 47 ± 5 m with localized thinning reaching up to 160 m (Muskett et al., 2003; Sauber et al., 2005).

The Malaspina Glacier is a temperate surging glacier, with surge cycles of 5 to 30

years for each of the three lobes separately (Post, 1969; Gustavson and Boothroyd, 1987; Muskett et al., 2008). Velocities on the lobes range from .5 to 1 m/d (Sharp, 1958; Krimmel and Meier, 1975; Lingle et al., 1997) during nonsurging flow; during surge conditions, velocities can reach 10 to 20 m/d (Molnia and Jones, 1989). A necessary precondition for surging is an increase of englacial water storage and build up of glacier ice that increases surface slope (Lingle and Fatland, 2003; Muskett et al., 2008). The most recent series of surges occurred in 1999-2002 with concurrent events on the Agassiz Lobe, Lower Seward Glacier and Seward Lobe, and Marvine Glacier (Muskett et al., 2008). This surge cycle was correlated with increased precipitation since 1976/77 that increased accumulation of ice and the volume of water stored within the glacier.

Oily Lake is a glacial dammed lake that is bound by the moraine bands of the Seward and Agassiz Lobes (Fig. 2). Drainage of water from glacial lakes and associated outburst floods can affect glacier flow dynamics, valley bottoms, cause substantial erosion, and increase glacier velocity. In 2003, Oily Lake was observed drained of water after a glacial surge, this indicates the interaction between Oily Lake and the Malaspina Glacier (Muskett et al., 2008).

Glacial Surface Features

Surface features on the glacier include foliation, crevassing, and folding (Sharp, 1958). Crevasses are widespread on the glacier surface, primarily vertical, .5 to 4 m wide, 20 to 25 m deep, and can span 100+ m in length. Transverse crevasses are located on the steep slopes of the glacier and form in response to ice flow and subglacial topography (Sharp, 1958). Radial crevasses are present on the Seward Lobe; these trend normal to the lobate borders, are more numerous, and converge toward the Lower Seward

Glacier throat, suggesting they form in response to the spreading of the ice over the piedmont (Sharp, 1958).

Glacial Topography

Several topographic maps and digital elevation models (DEM) are used to identify static topographic features on the glacial surface versus transient features formed by changing ice dynamics (Fig. 6). Determining the topography and surface slopes of the glaciers requires the use of elevation data acquired by several techniques and at several different times because there is no uniform and high quality elevation model that covers the entire study area. Elevation data obtained at different times can be used to check as to whether or not surface features are persistent or changing. Perturbations in topography that are persistent over time reflect features at the base of the ice.

Elevation data sets used for topographic analysis are: 15 minute USGS contour maps derived from 1972/73 air photos (www.usgs.gov), a 2- ARC second DEM from the National Elevation Dataset (NED) (http://ned.usgs.gov/NED/), several DEM's from the Shuttle Radar Topography Mapping (SRTM) mission (http://edcsns17.cr.usgs.gov/NewEarthExplorer/ and a specially processed elevation model provided by R. Muskett), and a DEM from ASTER GDEM, a new global DEM dataset introduced in 2009 (http://www.gdem.aster.ersdac.or.jp/).

For analysis of surface features, contemporary datasets are compared to the older USGS contour maps. The NED dataset is used for analysis of topography on the Upper Seward and Lower Seward Glaciers. SRTM data are used for inspection on the Seward Lobe, one DEM on the southern portion of the Lobe, and another DEM on a portion of the northern Seward lobe near the mouth of the Lower Seward Glacier. The ASTER

GDEM dataset contains anomalous elevations on the Lower Seward and Seward lobe and is used only to inspect the Agassiz Glacier.

The Upper Seward Glacier is located in the Seward Glacier Basin at elevations between 1500 m and 2000 m. The glacier discharges into the head of the narrow and sinuous Lower Seward Glacier and flows down the southern front of the Saint Elias Mountains and out onto the piedmont (Fig. 2A-C). The ice at the head of the Lower Seward Glacier is located at approximately 1500 m in elevation with the ice surface sloping at a 6º angle over a 150 m topographic step (Fig. 6B, UTM location 6.678). After this step, the surface slope decrease to 2º until the ice encounters another topographic step at approximately 1100 m in elevation (Fig. 6B, UTM location 6.669). The surface slope at the step is approximately 6º over 100 m of elevation. The ice then decreases in slope to 2º until it reaches the mouth of the Lower Seward Glacier where the slope steepens 3º before ice flows out onto the piedmont to become the Seward Lobe (Fig. 2B). Relief on the Seward lobe is nearly 500 m over a distance of ~ 40 km and the surface slope shallows to < 1º near the terminus.

The Agassiz Glacier begins in the high elevations (1500 m) on the southern front of Mount Saint Elias (Fig. 2D-F). In the upper portion of the Agassiz Glacier, the surface slopes at a 5º angle (Fig. 6C). The ice flows south down the valley and surface slope decreases to 1º to 2º until the ice flows over a series of topographic steps that begin at approximately 900 m in elevation (Fig. 6C, UTM location 6.670-6.665). The topographic steps slope approximately 4 º over 300 m in elevation. The steps terminate as ice moves out of the mountain front onto the piedmont. Topographic relief on the piedmont is 500 m over a ~ 20 km distance with a surface slope <1º.

Figure 6: Topography of the Malaspina Glacier system. A) NED 2-ARC second shaded relief image of the entire Malaspina Glacier and surrounding mountain ranges. Location of the profile lines are highlighted in red B) Airborne Terrane Mapper (ATM) profile of the Lower Seward Glacier. C) Profile of the Agassiz Glacier taken from ASTER GDEM.

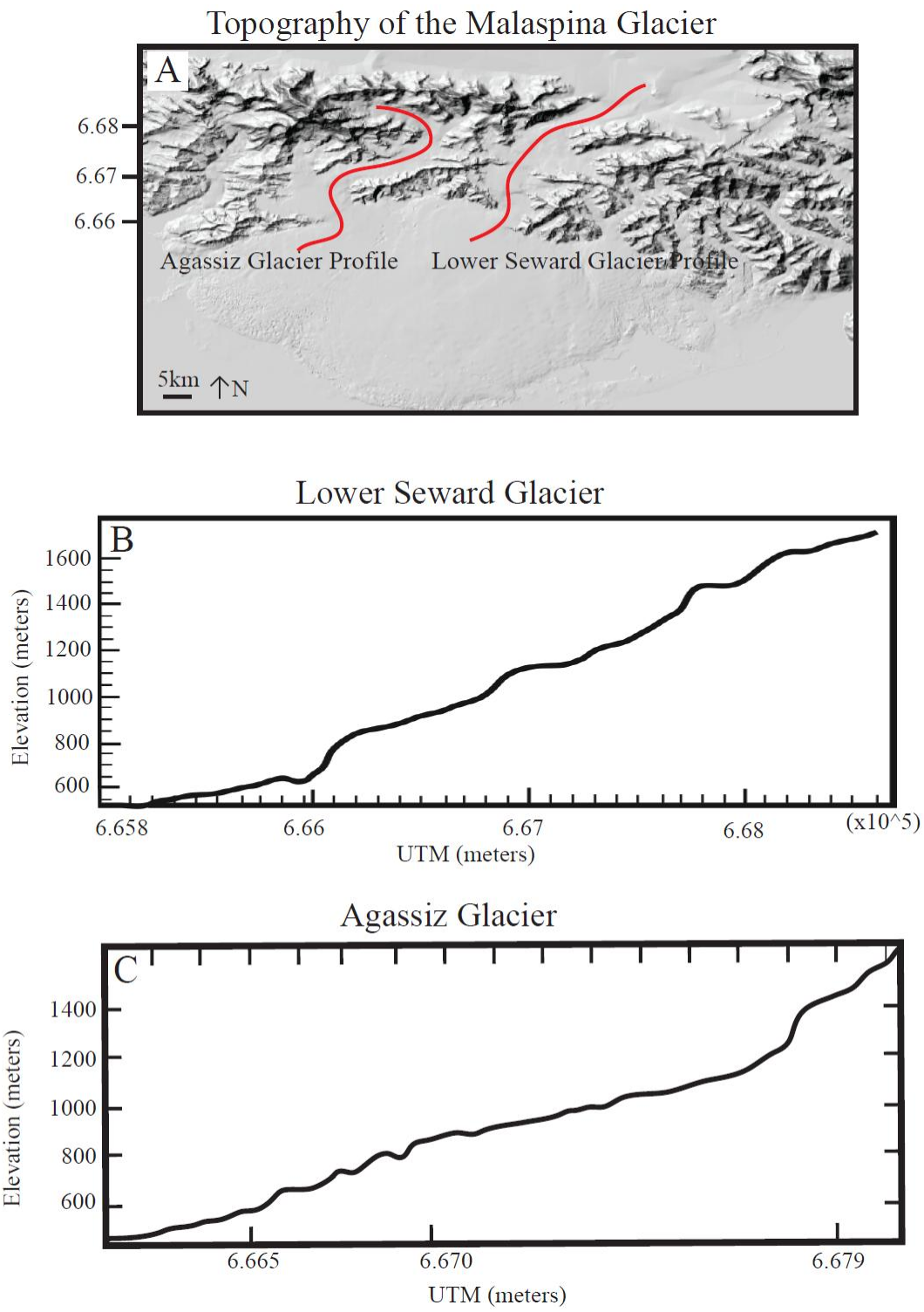
Topography of the Malaspina Glacier
A
6.68
6.67
6.66
Agassiz Glacier Profile
Lower Seward Glacier Profile
5km
N
Lower Seward Glacier
B
Elevation (meters)
1600
1400
1200
1000
800
600
6.658
6.66
6.67
6.68
(x10^5)
UTM (meters)
Agassiz Glacier
C
Elevation (meters)
1400
1200
1000
800
600
6.665
6.670
6.679
UTM (meters)

METHODS

Image Acquisition and Preprocessing

Images are chosen on the criteria of limited cloud and snow cover from roughly the same time of year with a similar sun angle and azimuth; these criteria maximize the similarity of surface features in the image. Most glaciers are found in areas of poor weather, making repeated acquisition of cloud free images difficult. Landsat's continuous record of acquisitions over the globe during the last three decades with repeat coverage of 16 days makes it an optimal sensor to acquire images of glaciers that can be compared at monthly and longer time intervals (http://landsat.gsfc.nasa.gov/about/L5_td.html).

For this study, several Landsat 5 Thematic Mapper and Landsat 7 enhanced Thematic Mapper images are acquired to track monthly and annual ice surface motion (Table 1). The images downloaded from the USGS Earth Explorer website are corrected (radiometrically and geometrically) to a level 1T as defined by the USGS (http://edcsns17.cr.usgs.gov/helpdocs/landsat/product_descriptions.html#systematic_l5_l1g).

The Landsat scenes are resized to subsets that encompass the study area. Dark subtraction is applied to radiometrically correct the images. Dark subtraction is a method that subtracts a minimum brightness value or a calculated average minimum brightness value from every pixel and multiple spectral bands of an image. The minimum value is determined from selected pixels in the image that should have zero reflectance, such as

pixels over still water. The subtracted minimum value represents contributions from the atmosphere that may have increased pixel brightness values in the image (Jensen, 2005).

Optical Feature Tracking

The velocity, topography, structures, and strain rates of a glacier are influenced by the geometry and mechanical properties of the material at its base, including bedrock, unconsolidated till, and fluvial deposits (Fowler, 1982; Boulton and Hindmarsh, 1987; Gudmundsson, 2003). Topographic features at the base of a glacier will modify ice flow direction and magnitude, but the effects become attenuated as they propagate upwards through the ice. To determine the underlying topography and structural geology, the surface topography, flow velocity, and surface features are analyzed using several remote sensing techniques. The approach follows that used by Bruhn et al. (2010) to explore relationships between ice flow and bedrock geology on the Bering Glacier.

The velocity and strain rate fields on the surface of the glacier are determined from changes in the position of features that appear on two geographically coregistered images acquired at different times. In practice, the displacements are found at points on a regular grid that is superimposed on the older of the two images. A small patch of pixels centered on each grid point is matched as best as possible with a similar patch of pixels on the second image, and the displacement is the difference in coordinate positions of the centers of the correlated patches. This process is repeated for each point on the grid to create a set of displacement vectors on the surface of the ice. If a displacement vector cannot be resolved at a specific grid point because of poor correlation or an obvious error in correlation, then the displacement at that point is approximated by interpolation using the displacements at neighboring points. The displacement at each point divided by the

time between acquisitions of the images is an estimate of the velocity magnitude. The components of the strain rate tensor at each grid point are then found from the spatial derivatives of the velocity field, using a finite difference approximation to calculate Cauchy's deformation tensor (Cardozo and Allmendinger, 2009).

Three computer programs are used to implement the processing steps outlined in the previous paragraph. The displacement vector field is determined using Coregistration of Optically Sensed Images and Correlation software (COSI-Corr), obtained from the Tectonic Observatory group at the California Institute of Technology (Leprince et al., 2007a,b). Editing of the displacement vectors is done using software written by the authors in the Matlab © scripting language. Strain tensors are computed from the edited velocity field using SSPX software written by Cardozo and Allmendinger (2009).

COSI-Corr

The algorithm implemented by the COSI-Corr software uses a phase difference technique to obtain a measure of similarity (correlation) between parts of two images. Pixel subsets extracted from both images are converted into the frequency domain by applying the Fast Fourier Transform. The phase spectrum of the second image subset is multiplied by the complex conjugate of the phase spectrum of the reference (first) image and then divided by the absolute value of the spectral product. The inverse Fourier Transform of this normalized cross spectrum produces a correlation peak; the coordinates of this peak provide the relative offset of a local 'feature' between the two images (Shekarforoush et al., 1996; Leprince et al., 2007a). This method is resilient to image noise because a single coherent correlation peak is the choice for coregistration and noise distributed amongst other incoherent peaks can be assumed to have a mean value of

zero (Shekarforoush et al., 1996).

This phase spectrum correlation routine requires specification of the size of the search window within which correlation will be attempted, the step or grid spacing size, and the acceptable signal-to-noise ratio below which correlation will fail. The window size defines the size of a sliding window that passes over the image and correlates points. The window size can be a fixed dimension or scaled to a maximum and minimum window. When the window is multiscaled, the larger window is correlated first and if correlation is successful, the correlation algorithm is re-executed on a smaller scale. This process is iterated until correlation fails or the minimum window size is reached. The step size determines the distance in pixels between the sliding windows. The SNR is the height of the correlation peak to the background noise, and measures the robustness of each correlated value (Ayoub et al., 2009).

No specific set of parameters is used when correlating images; the algorithm implemented in COSI-Corr is flexible to allow processing of any digital image acquired in any part of the electromagnetic spectrum (Leprince et al., 2007a). Each parameter must be adjusted to the specific image pair to obtain the best correlation. Large windows produce displacement fields with less noise from inaccurate correlations but lose details within the velocity field. Smaller window sizes produce finer detailed velocity fields but also include more noise from miscorrelations. Trial and error adjustment is required to determine the parameters best suited for correlation of specific image pairs (Leprince et al., 2007a, b,).

Scaling of windows sizes was needed to produce an accurate velocity field. On images that are acquired a year or more apart, ice displacements can be over 100+ m

and larger window sizes are needed. Smaller window sizes are used when correlating images on shorter timescales. Multiscaled windows are successful at tracking the motion of glacial ice because the surface features frequency and size are not uniformly distributed over the glacier. The larger windows retrieve displacements in the noisy areas of the images, and the smaller windows in less noisy areas. The best parameters were chosen individually for each image pair on the basis of how well the calculated flow field matched the expected flow of ice, which flow fields had the least amount of miscorrelations or outliers, and if the calculated magnitudes of displacements were similar to manually measured displacements.

Band 2 on the Landsat 5 TM and Landsat 7 ETM+ was chosen to run all correlations on. Band 2 lies within in the visible range of the electromagnetic spectrum (wavelengths from .52 to .60 μm); within this range of wavelength, spectral reflectance curves for snow, glacier ice, and dirty glacier ice show the greatest difference in reflectance (Zeng et al. 1984; Winther, 1993). This difference in reflectance is useful to highlight distinct features and differences on the surface of the glacier that can be used to track ice motion from year to year. Bands in the near infrared range are not used because reflectance from glacier ice and dirty ice is similar, making features from clean and dirty ice that could potentially be tracked harder to distinguish.

The COSI-Corr algorithm is unbiased because it does not account for a known direction of motion, and can therefore produce displacements that are anomalous to actual ice movements. Visual inspection of the displacements is done utilizing a script written in the Matlab programming language. If a vector direction or magnitude is significantly different than those at the surrounding grid points it is removed and

replaced by an interpolated vector calculated using displacement components from grid points in the surrounding region. This method preserves the majority of computed vectors while producing a coherent vector field free of noise from anomalous vectors.

Coregistration of the images in geographic coordinates is checked by alternating or 'flicking' between images on the computer display screen. If the images are approximately coregistered, there is little or no apparent motion of rock or bare ground. If the image pairs pass this visual inspection test, then several correlations are run to quantitatively evaluate misregistration at subpixel scale between image pairs. The calculated offset in the images is no more than 2 m or $1/15^{th}$ of a pixel in any of the image pairs.

Strain Rate

The strain rate field on the surface of the glacier is calculated from the edited velocity grid, using an algorithm implemented in the SSPX software (Cardozo and Allmendinger, 2009). Displacement gradients are calculated at each grid point to produce a two-dimensional deformation tensor that relates the quadratic elongation of a line (Λ) following deformation either to the orientation of the line before (Green's Tensor) or after (Cauchy's Tensor) deformation. The eigenvalue and eigenvectors of Cauchy's Tensor are the inverse values of the principal quadratic elongations ($\Lambda 1$ and $\Lambda 2$) at each grid point, which are in turn the squared values of the maximum and minimum principal stretches S1 and S2, where Si (i = 1,2) is the square root of the Λi. The principal strains are embedded in the stretches as Si = (1 + **e**i), where **e**i is longitudinal strain. The orientations of S1 and S2 correspond to the axes of principal strain. When the longitudinal principal strains are divided by the time between acquisitions of the images, we obtain an estimate of the

principal strain rates at each grid point. These rates are typically on the order 10^{-9} s^{-1} or less, which implies that the strain rate axes may lie subparallel to the principal axes of stress as discussed by Bruhn and Haeussler (2006). In this situation, we expect brittle fracturing that forms crevasses to propagate parallel to the direction of maximum shortening strain rate.

The results of the velocity and strain rate calculations are presented as maps of the velocity and dilatational strain rate fields. Directions and relative magnitudes of velocities are shown by vector or 'arrow' plots, with the tails of the arrows located at the grid points. Contour maps of velocity magnitude are also created with units of m/month to m/year, depending on the time span between image pairs. The dilatational strain rate is also displayed on contoured maps; this rate is positive if the area surrounding the grid point is dilating and negative if the area is contracting. The dilatational strain rate is the product of (S1xS2)/time. The orientation of the axis of principal maximum shortening rate is plotted as a dark blue line centered about each grid point.

The above method only calculates a two-dimensional velocity and strain rate field whilst in nature; ice flow is three dimensional as noted by Sharp in his discussion of the formation of foliation and folds on the Malaspina Glacier (Sharp, 1958). The results of this study therefore only reflect velocity and strain on the surface of the glacier.

Glacier Analog Modeling

To investigate how glacial ice would respond to underlying topographic features, a glacial analog model is used (Fig. 7). A pseudo ice valley was constructed from Plexiglas to model a glacial ice valley. To represent the geometry and dynamics of a glacier ice valley, the model was scaled following the principles discussed by Hubbert

(1937). The model is scaled at a ratio of $2x10^5$, thus 2 cm on the model is equivalent to 1 km in nature. Flubber is an analogue for glacial ice and is a viscoelastic material that flows plastically under low stresses but is brittle and fractures under high stresses much like ice (Gerbi, 2003). To model underlying topography, scaled insets of topographic features, carved from Styrofoam, are placed on the bottom of the model (Hubbert, 1937; Aydin and Nur, 1982). Flubber is placed over the models and allowed to flow freely down the "glacial valley" at an angle of 2º. Dots are placed on the surface, before flow begins, in an evenly spaced grid and tracked to create flow fields for the glacier. Flow fields generated from physical experiments were compared to results on the glacier. The topographic models used in this study are a ridge oriented obliquely to ice flow at a 45º angle (Fig. 7A) and a ridge oriented parallel to ice flow (Fig. 7B).

Table 1

Image Data

Image Number	Acquisition Data	Scene Number	Row	Path
1	September 11, 1986	L5062018_0181986091	18	62
2	August 29, 1987	L5062018_01819870829	18	62
3	September 4, 1995	L5062018_01819950904	18	62
4	September 27, 1995	L5063018_01819950927	18	63
5	July 28, 1999	L71063018_01819990728	18	63
6	August 2, 2001	L71063018_01820010802	18	63
7	July 19, 2007	L5062018_01820070719	18	62
8	August 11, 2007	L5063018_01820070811	18	63

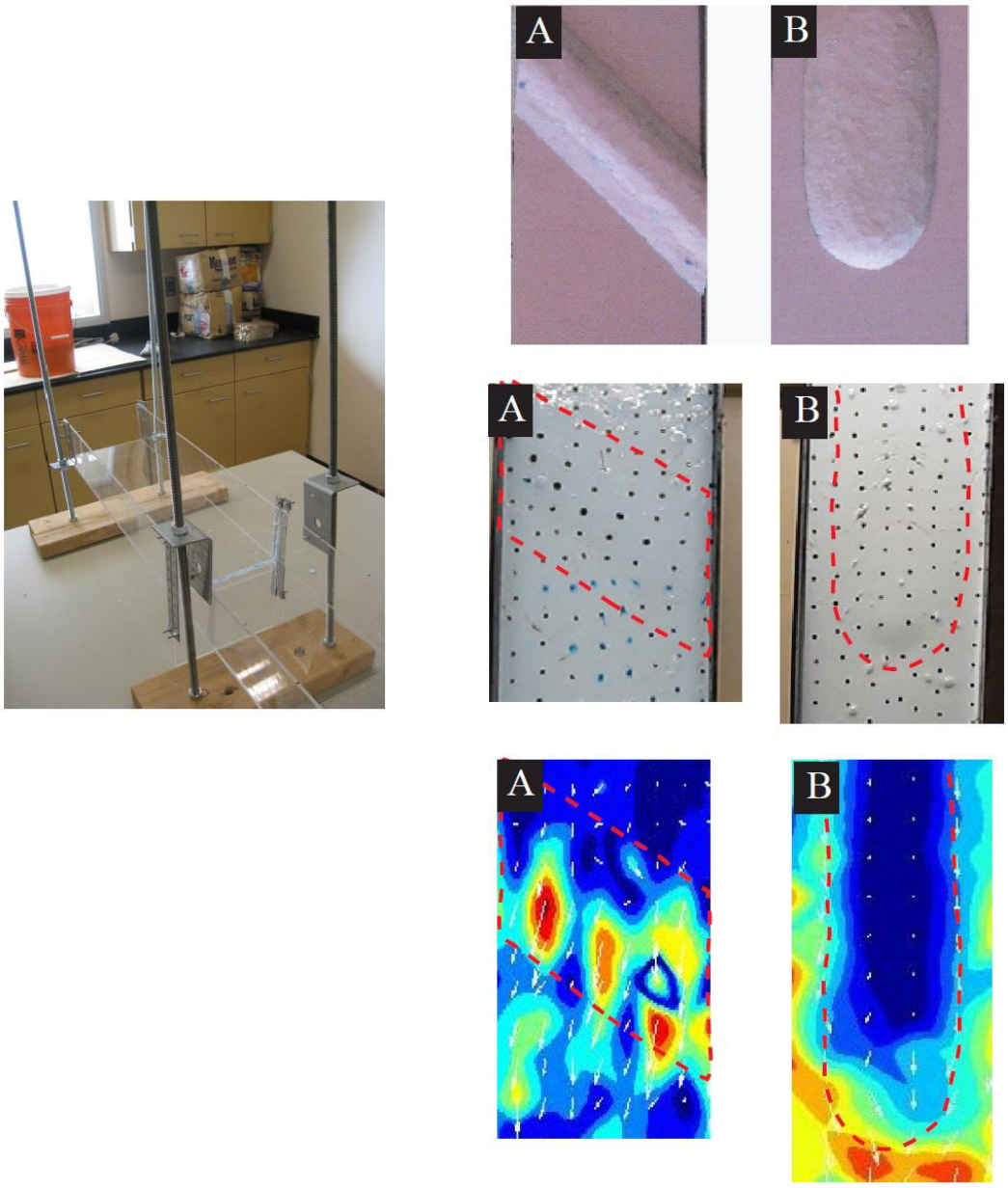

Figure 7. A scaled glacial analog model constructed to understand how ice may respond to underlying topography. Flubber is placed over the topographic models with a grid of evenly space points marked on the surface to track surface flow. A) A ridged placed at a 45 degree angle. B) A ridge placed parallel to ice flow.

RESULTS

Glacier Modeling

Flow patterns from the physical model illustrate how ice on the glacier may respond to an underlying ridge, aiding in the interpretation of the feature tracking results. The pattern of flow as the flubber moves over the ridge shows that ice increases in speed on the down slope of the ridge (Fig. 7A). This implies that if this pattern is seen on the feature tracking results, the ice is likely responding to an underlying ridge or topographic step. The pattern of flow for a parallel ridge shows the ice flow slowing over the ridge with most of the ice motion being deflected and increased around the edges of the ridge and at the front of the ridge (Fig. 7B). This suggests that velocities over a ridge parallel to ice flow would show the pattern of slower velocities over the ridge with faster velocities deflected around the region of slower flow.

Upper Seward Glacier

Surface velocity maps of the Upper Seward Glacier are generated from a 1-year correlation with Landsat 5 TM images from September 11, 1986 and August 8, 1987 (Table 1, Fig. 8). The surface flow field in this study is comparable to that found by Ford et al. (2003), which calculated velocity from Interoferometric Synthetic Aperture Radar (InSAR). The surface velocity maps of the Upper Seward Glacier show that velocities in the western portion of the glacier flow at a faster rate than those in the eastern portion of the glacier, with flow being subdivided by a northwest trending ridge (Fig. 8). This ridge

is marked by a series of nunataks and crevassing along the length of the ridge (Fig. 8A).

Ice in the western portion of the Upper Seward Glacier flows west to east at a rate of 0 to 300 m/yr. Faster velocities are located along the southern side of the glacier (100-300 m/yr) and slower velocities (0-100 m/yr) are located along the northern side of the glacier (Fig. 8). A subtle topographic feature that trends east-west subdivides the flow in the region of the glacier as documented by Ford et al. (2003). As the ice continues east, flow is deflected towards the southeast where it encounters the northwest trending ridge; velocities increase rapidly to 400 to 600 m/yr before the ice flows into the head of the Lower Seward Glacier (Fig. 8).

The ice in the eastern portion of the Upper Seward Glacier flows at a much slower rate (0-50 m/yr) towards the southwest (Fig. 8B). The ice is diverted toward the head of the Lower Seward Glacier as it encounters the northwest trending ridge. Before flowing into the Lower Seward Glacier, velocities reach up to 300 m/yr. Ice from the eastern and western Upper Seward Glacier converge at the head of the Lower Seward Glacier.

Lower Seward Glacier

Velocity maps of the Lower Seward Glacier were created from Landsat 5 TM images acquired a month apart for the years 1995 (September 4, 1995 to September 27, 1995) and 2007 (July 19, 2007 to Aug 11, 2007) (Table 1). The flow fields from 1995 and 2007 exhibit similar velocity patterns in both direction and magnitude (Fig. 9). This suggests that the displacement field on the surface of the ice is being influenced by bedrock topography and underlying geology and departs from a simple pattern of down glacier flow. To discuss how glacial ice is moving down glacier, the velocity image is subdivided into three regions.

Zone S-1

Zone S-1 is located where ice from the Upper Seward Glacier flows into the Lower Seward Glacier over a topographic step at an elevation of 1500 m (Figs. 6 and 9). Ice flowing over the topographic step reaches rates of up to 60 m/month (Fig. 9). Moving south down glacier, faster velocities (40-60 m/month) are located in the eastern portion of the glacier above the trace of the underlying Cascade Glacier Thrust Fault, with the surrounding ice flowing at a slower rate (10-20 m/month) (Fig. 9). Where ice flows over the topographic step, crevasses trend perpendicular to ice flow direction (Fig. 10A). Where surface slope and velocities decrease, two types of crevasses are found on the glacier surface: marginal crevasses that trend up glacier oriented obliquely to the glacier walls and longitudinal crevasses that are oriented parallel to glacier walls (Fig. 10A).

The channel of increased velocities in the eastern region of the glacier may be the surface representation of the Cascade Glacier Thrust Fault as ice preferentially erodes into the faulted and fractured rock in the subsurface.

Zone S-2

The northern portion of zone S-2 contains velocities in the range of 20-50 m/month. Moving south, the glacier flows over a topographic step at approximately 1100 m in elevation and surface velocities increase rapidly down glacier, flowing at rates of 70-100 m/month (Figs. 6 and 9). Velocities below the topographic step decrease to 50-60 m/month. Transverse crevasses form on the surface of the glacier over the topographic step and where velocities are the fastest (Fig. 10B).

The pattern of flow over the topographic step in zone S-2 compares to the analog model results where increased velocities occur on the down slope of the ridge (Fig. 7A).

Coincident with the topographic step is the trace of the Dome Pass and Chaix Hills faults (Fig. 11). Here Cretaceous metamorphic rocks of the Yakutat Group are faulted over the top of Tertiary sedimentary rocks of the Poul Creek Formation, which in turn are faulted over the sedimentary rocks of the Yakataga Formation and Yakutat Group in the footwall of the underlying Chaix Hills Fault (Fig. 11). There is no evidence for recent activity on the Dome Pass and Chaix Hills Thrust Faults and they are presumed to be inactive structures that were once linked to dextral shearing along the transform fault boundary and thrust belt to the southwest. The faults are exhumed by displacement and uplift above the Esker Creek, and Malaspina Faults (Bruhn et al., 2004; Bruhn et al., in press). Due to the inactivity on these faults, the formation of the topographic step is most likely caused by differential erosion rather than uplift from tectonic activity.

Zone S-3

Within zone S-3, higher velocities are present near the margins of the glacier with regions of decreased velocities near the centerline of the glacier (Fig. 9). Velocities near the center of the glacier range from 10-50 m/month increasing to upwards of 80 m/month near the glacier margins (Fig. 9). The glacier flows at a rate of 50-80 m/month before discharging into the Seward Lobe where the velocity decreases to 10-20 m/month. Fast flow out of the mouth of the Lower Seward Glacier corresponds to a steepening of the topography above the piedmont (Fig. 9). Crevasses in this region are predominately transverse and marginal (Fig. 9C).

The pattern of slower velocities near the centerline of the glacier with velocity increasing towards the margin is similar to the flow pattern observed on the analog model of a ridge oriented parallel to ice flow (Fig. 7B). Ice in zone S-3 is flowing over the rocks

of the Yakutat Group. These rocks are exposed on both sides of the glacier valley and are a tightly folded and faulted unit (Fig. 11). The flow pattern is presumably caused by differential erosion of the underlying rock within the Yakutat Formation, possibly related to erosion along folded bedding surfaces which created an elongated dome shaped ridge of bedrock with the long axis aligned down slope.

Strain on Lower Seward Glacier

Strain rates calculated from the velocity field are shown in Fig. 12. Areas highlighted in red are regions on the ice surface that are undergoing dilation of surface area, while areas of blue are contracting in surface area. Areas of the greatest dilatational strain rate are located where the velocities are fastest and the slope of the glacier is steepest, like that in the region at the head of the Lower Seward Glacier, the Chaix Hills Fault, and the topographic step just above the mouth of the Lower Seward Glacier (Fig. 12).

The blue lines indicate the axis of principal maximum shortening rate and should be aligned parallel, or nearly parallel, to the crevasses that propagate in the direction of maximum contraction within the ice (Harper et al., 1998). The orientations of the axes of maximum shortening for the Lower Seward Glacier mirror the crevasses that form on the surface of the glacier (Figs. 10 and 12). This observation provides an independent check on the validity of the velocity field obtained by feature tracking

Agassiz Glacier

The Upper Agassiz Glacier

Velocity fields for the upper Agassiz Glacier were generated from Landsat 5TM images acquired on September 4, 1995 and September 27, 1995 (Table 1, Fig. 13). The upper Agassiz Glacier flows down the southern flank of Mount Saint Elias between the elevations of 1500 m and 1100 m. In this region, the glacier's surface slopes at a 5º angle, and the velocities range between 20-90 m/month (Fig. 6). The velocity is greatest in the central part of the glacier and decreases outward toward the margins (Fig. 13). Crevasses on the surface are predominately transverse and marginal (Fig. 14). The axes of maximum shortening strain rate are oriented approximately subparallel to the crevasses on the surface of the ice, validating the velocity field in the upper portion of the Agassiz Glacier (Figs. 14 and 15).

The Central Agassiz

The central part of the Agassiz Glacier is located between elevations of 1100 m to 500 m. In the upper portion of the central Agassiz Glacier, the surface slopes at 1º- 2º along the northern side of the Samovar Hills (Fig. 6). Velocities decrease in this region from those of the upper Agassiz Glacier to rates of 10-15 m/month with several areas of faster velocities (30-50 m/month) located above the trace of the Chaix Hills Fault and down the centerline of the glacier (Fig. 16). A 1-year correlation done on Landsat 5 TM images from the dates September 11, 1986 to August 29, 1987 show the same region of higher velocities, with the main body of the glacier flowing at 100 to 200 m/year and faster regions flowing at 400-600 m/year (Table 1, Fig. 17). Prominent crevassing is not present on the surface in the upper portion of the central Agassiz Glacier, but the strain

rate map shows dilatational strain that corresponds to the regions of faster flow above the underlying Chaix Hills Fault (Fig. 15).

Where the glacial ice bends through a 90º angle around the tip of the Samovar Hills, several topographic steps are present on the ice. The steps dip at an angle of 4º over 300 m in elevation (Fig. 6). The surface velocities in this area range from 10 to 25 m/month or 100-200 m/year (Figs. 16 and 17). The surface of the glacier is broken by transverse, longitudinal, and marginal crevasses where it flows over the steps (Fig. 14). Ogives initiate at the base of the topographic step and create a prominent striping of the glacier that continues to the terminus (Fig. 18). The strain rate map shows dilatational strain below the topographic step on the glacier and shortening axes trend roughly parallel to the crevasses (Figs. 14 and 15). The initiation of the topographic steps corresponds to where the Chaix Hills Fault is oriented oblique to ice flow and the Kultieth Formation is thrust on top of the Yakataga Formation (Fig. 19). Below the topographic velocities range from 10-25 m/month or 100-600 m/year (Figs. 16 and 17), with fastest flow contained on the western side of the glacier. This may be explained by a gentle 1 º westward dip on the glacier surface from the Samovar Hills toward the Chaix Hills, and mimics the tilting of bedrock bedding surfaces in this area. Before ice flows out of the mountain front onto the piedmont, the glacier surface slopes at 4º and flows over the trace of the Malaspina fault (Fig. 19).

The Agassiz Lobe

Ice discharges onto the piedmont from the upper and central part of the Agassiz Glacier to form the Agassiz Lobe of the Malaspina Glacier (Fig. 2F). The ice on the Agassiz Lobe flows at a rate of 6-22 m/month or 100-400 m/yr (Figs. 17 and 20). The

fastest moving ice is located in the central portion of the Agassiz Lobe and flows in an arcuate path towards the west. Surface velocities in the moraines to the east of the glacier lobe do not show this westward trend in flow: rather, they are directed south parallel to the moraine bands (Fig. 21). The westward deflected flow may be indicative of the uplift and tilting of the Chaix Hills and Samovar Hills by displacement on the Malaspina fault, or indicate uplift on a new incipient fault under the piedmont (Bruhn et al. 2004; Chapman et al., in press). This subdivision of velocities may also indicate the presence of a subglacial ridge beneath the Agassiz and Seward Piedmont, which trends subparallel to the Malaspina fault.

The Seward Lobe

To determine velocities on the Malaspina Lobe feature tracking was done using Landsat 5 TM images from September 11, 1986 and August 29, 1987 and Landsat 7 ETM+ images from July 28, 1999 and August 2, 2001 (Table 1). The attempt to track features over a period of 1 month failed because the movement of ice in this region was too small to be tracked by COSI-Corr's search window. However, velocities were obtained for several parts of the glacier over a period of 1 to 2 years (Fig. 22).

The most distinct flow feature on the Seward Lobe is a prominent tongue of faster moving ice that extends southward from the mouth of the Lower Seward Glacier towards the terminus near the coast. The ice on the Seward Lobe moves at a rate of 200-300+ m per year in the faster tongue and 100-150 m per year in the surrounding areas of the glacier (Fig. 22). This tongue of rapidly flowing ice was also observed from feature tracking done on synthetic aperture radar (SAR) images (Burgess et al., 2010).The tongue of faster velocities corresponds with the location of a ~10 km wide and ~250 m deep

trough at the base of the glacier detected by ice penetrating radar (Fig. 23a) (Conway et al., 2009). The area of increased flow also corresponds to surface depressions seen on an SRTM image of the Lower Seward Lobe; these depressions appear to overlie englacial or subglacial conduits through which glacial melt water may discharge (Fig 23b).The surface depressions when traced up glacier toward the mouth of the Lower Seward Glacier transition into the topographic ice ridge, or 'tongue', on the glacier (Fig. 24). This transition likely occurs as ice builds up when discharged out of the mouth of the Lower Seward Glacier then, as ice spreads out over the piedmont, this ridge disappears and becomes a depression on the surface, likely responding to subsurface channels or subglacial conduits beneath the surface of the ice.

A noteworthy feature on the Seward Lobe is a westward offset of ice flow. This is observed in a deflection of the raised ice ridge (Fig. 24) and the offset of the tongue of fast flow observed on the Seward Lobe when projected northward. This deflection occurs where the ice exits the mouth of the Lower Seward Glacier and crosses the Esker Creek Fault. The ice appears to have a 1-2 km offset towards the west.

Oily Lake

As ice flows outward from both the Lower Seward and Agassiz Glacier, it is directed northward towards an area of lower elevation along the base of the Samovar Hills and into Oily Lake (Fig. 25). Ice flowing out from the Agassiz Glacier into Oily Lake moves at a rate of 30-50 m/yr and ice flowing from the Lower Seward Glacier into Oily Lake moves at a rate of 10-40 m/yr. Radial crevasses around the margins of the lake and calving of ice into the water suggests that the lake extends subglacially (Capps et al., 2010) (Fig. 26). Pits that vary in diameter from tens to hundreds of meters wide and are

approximately 10-40 km deep are located on the surface of the glacier and extend south from Oily Lake along the moraine band that separates the Seward and Agassiz Lobes (Fig. 26). The pitting on the surface of the moraine band is similar to karst topography and suggests the collapse of the surface ice into englacial/subglacial conduits that drain water from Oily Lake. The pits extends south down the moraine band towards the location of Yana Stream, a discharge point for glacial melt water at the terminus (Fig. 26).

Oily Lake is located at the intersection of the Malaspina and Esker Creek faults, which intersect at roughly a 45° angle within the structural groin of the Samovar Hills (Figs. 4 and 25). The Malaspina and Esker Creek faults are currently active and generate earthquakes (Bruhn et al., 2004; Plafker and Thatcher, 2008). Activity on these faults presumably causes the surrounding rocks to become highly fractured, making glacial quarrying more efficient and forming a topographic low were Oily Lake now resides (Hallet et al., 1996).

`Figure 8. Velocity results for the Upper Seward Glacier generated from a correlation done between September 11, 1986 and August 8, 1987. A.) Composite Landsat Thematic Mapper image (bands 4, 3, 2) with an overlay of velocity vectors. Vectors are deflected around an underlying northwest trending ridge, marked by the nunataks that are northeast of the mouth of the Lower Seward Glacier. B.) Color scaled velocity magnitude image of the Upper Seward Glacier. The red line represents an outline of the Upper Seward Glacier Basin. Refer to Fig. 2A for location.

A.)

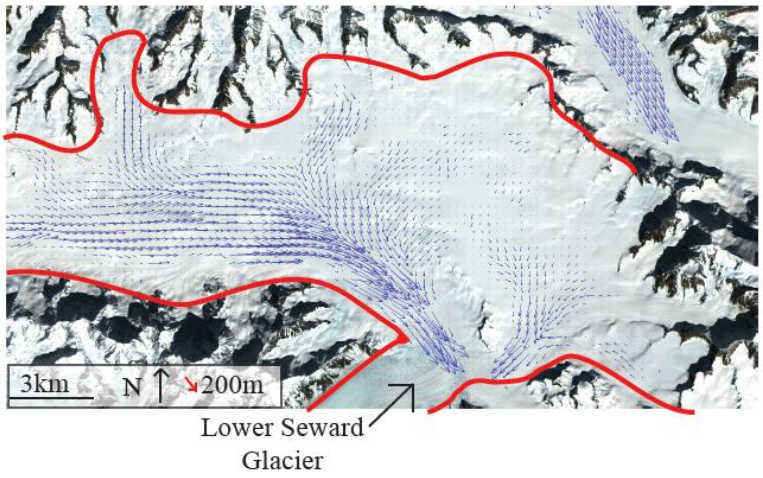
3km
N
200m
Lower Seward
Glacier

B.)

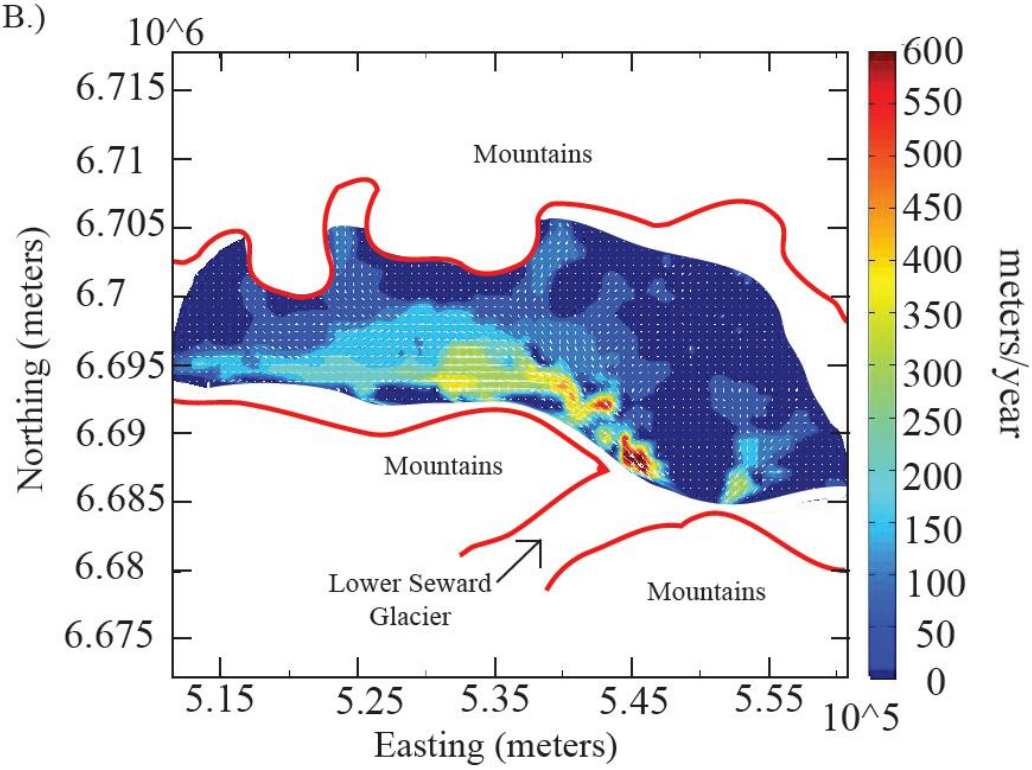
10^6
6.715
6.71
6.705
6.7
6.695
6.69
6.685
6.68
6.675
Northing (meters)
Mountains
Mountains
Lower Seward
Glacier
Mountains
5.15
5.25
5.35
5.45
5.55
10^5
Easting (meters)
600
550
500
450
400
350
300
250
200
150
100
50
0
meters/year

Figure 9. Color scaled velocity magnitude image showing ice motion on the Lower Seward Glacier for the years 1995 and 2007. For the year 1995, ice displacements are measured from September 4 to September 27 and for the year 2007, from July 19 to August 11. Images are subdivided into three regions; S-1, S-2, and S-3, with red outline representing the outline of the glacier. Refer to Figure 2B for location.

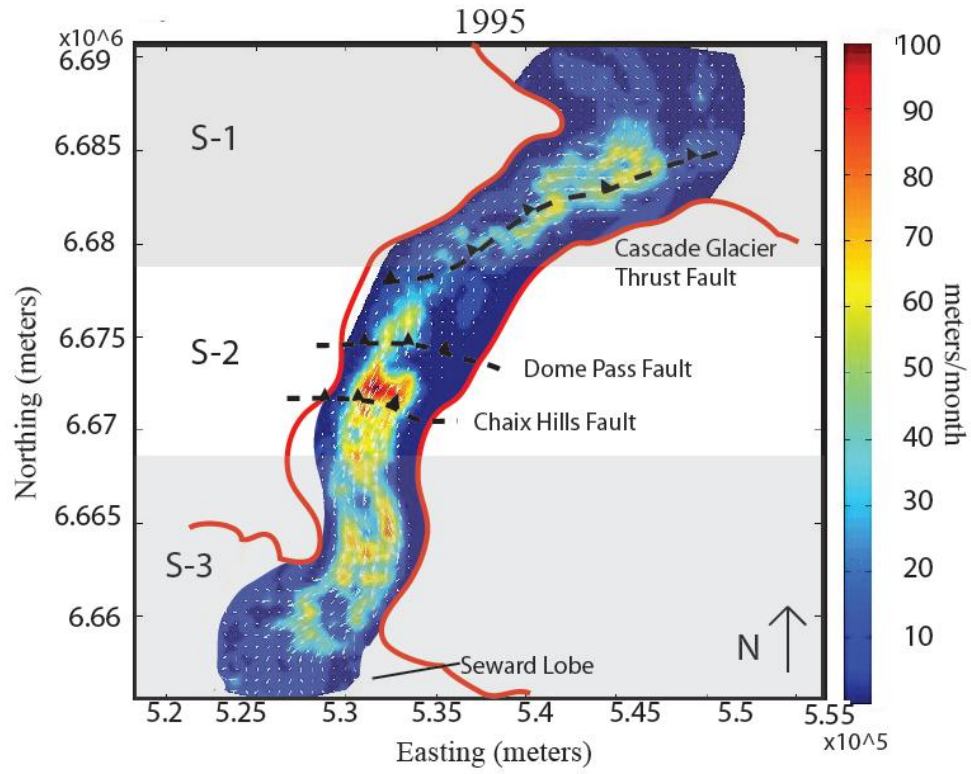

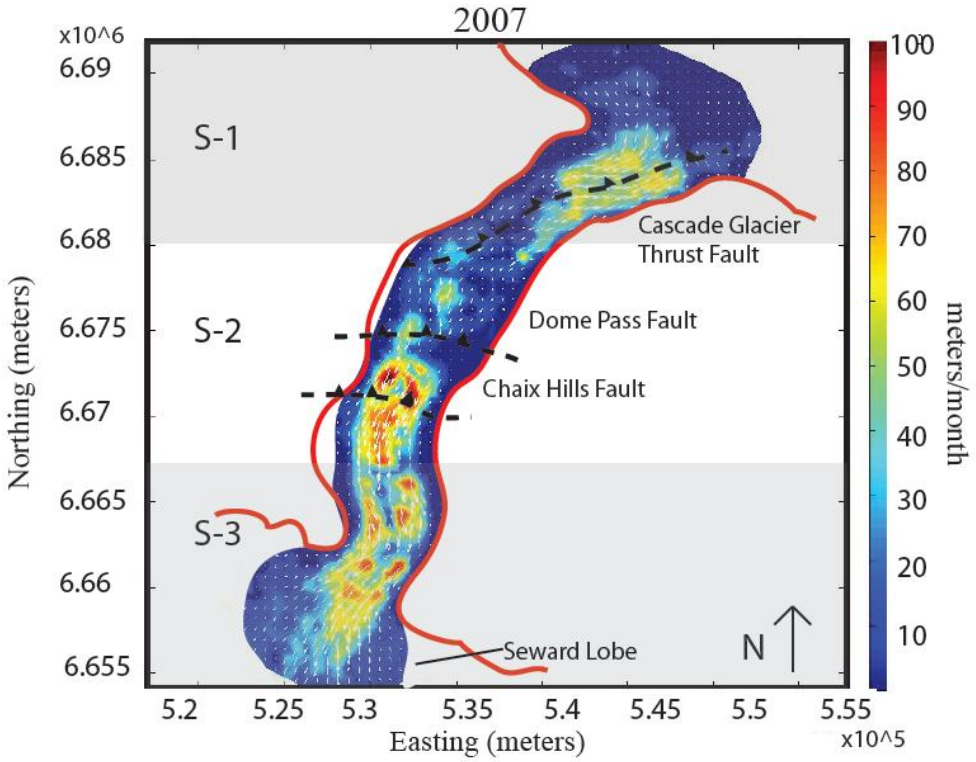

▲ – ▲ – ▲ – Thrust fault trace concealed beneath the ice.
Barbs on upper plate.

Figure 10. Crevasse images on the Lower Seward Glacier. Base image is a composite Landsat 5 Thematic Mapper image (bands 4, 3, 2). Subsets are KH-4 Corona satellite images that have been converted to black and white and enhanced to highlight the crevasses patterns. Crevasses are represented by black lines on the surface of the glacier.

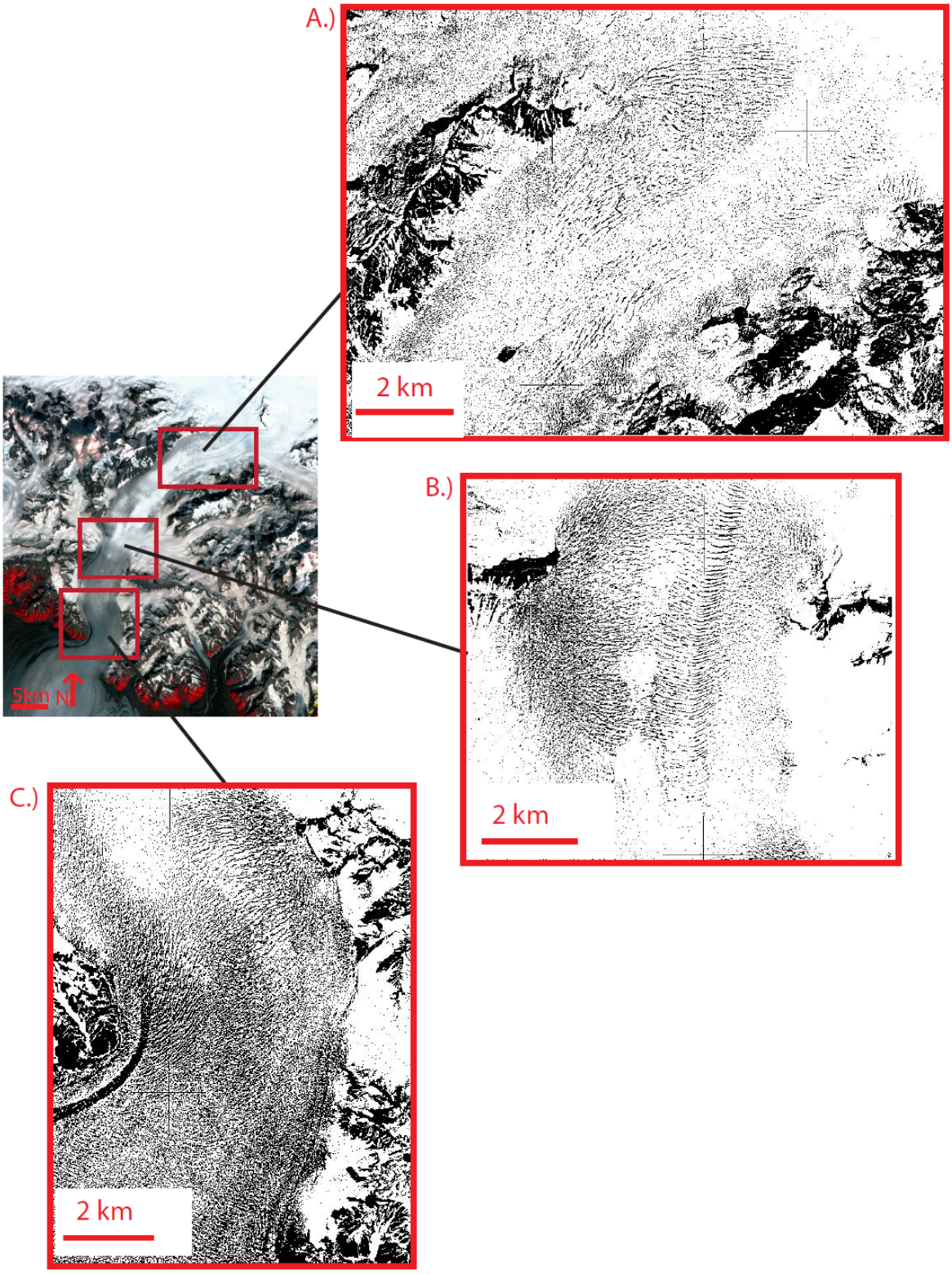
A.)
2 km
B.)
2 km
C.)
2 km
5km N

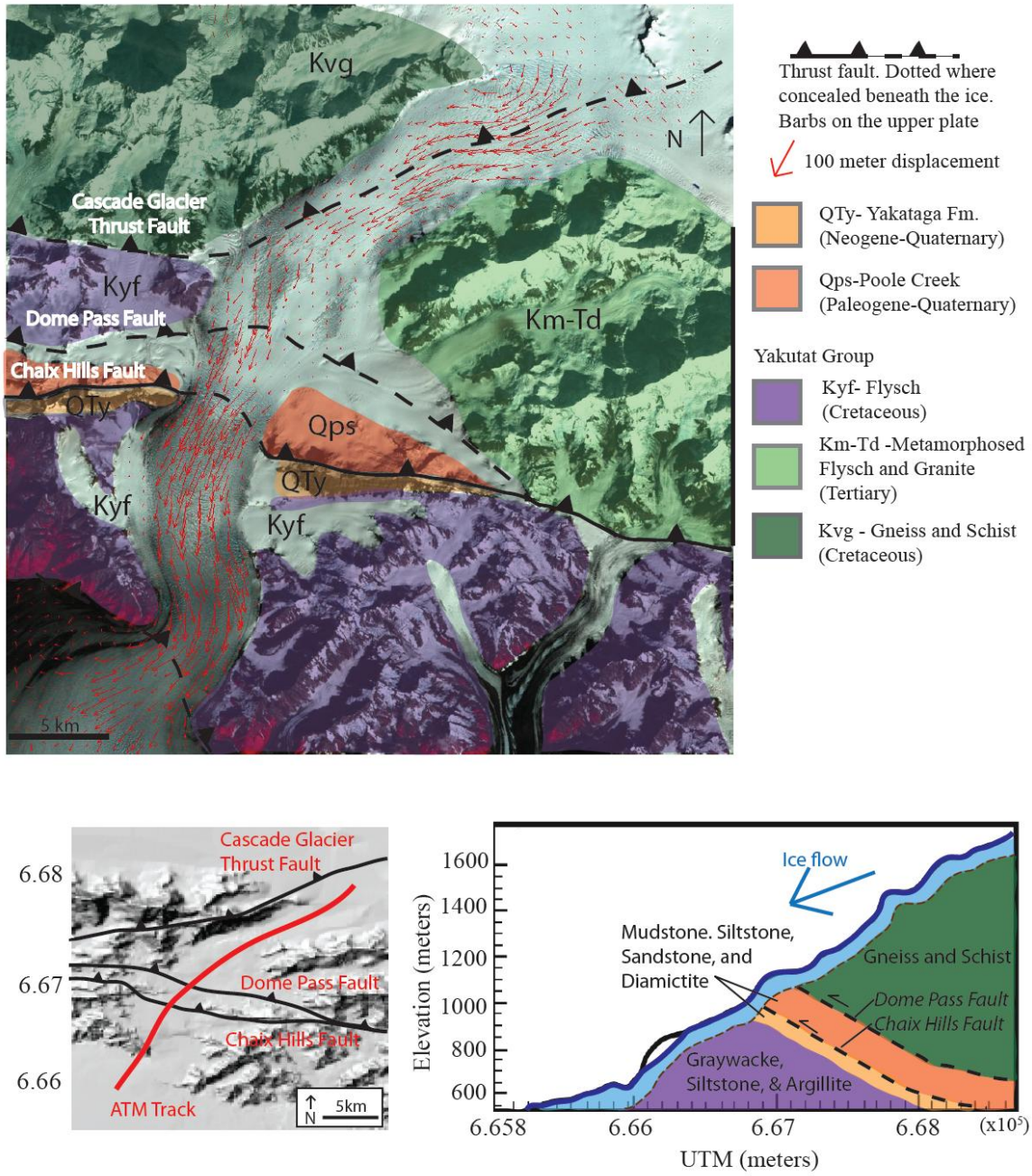

Figure 11.Geology surrounding the Lower Seward Glacier. A) Geology of the Lower Seward Glacier with velocity results overlain on a Composite Landsat Thematic Mapper image (bands 4, 3, 2). Vectors on the surface of the ice are generated from a correlation done from September 2, 1995 to September 27, 1995. The locations of major geologic structures are approximated beneath the ice. B) A topographic profile of the Lower Seward Glacier with the geology inferred beneath the surface of the ice.

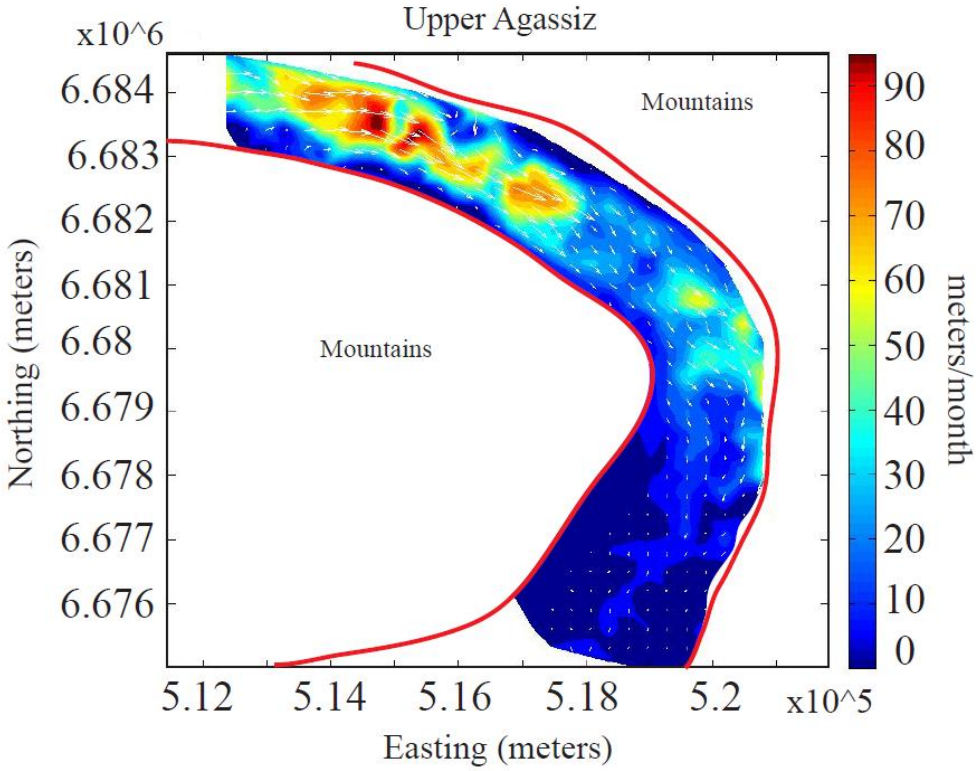

Figure 12. Strain rate map for the Lower Seward Glacier. Areas in red are undergoing dilation, areas in blue are undergoing contraction and blue lines indicate axis of maximum shortening. Red line represents the outline of the Lower Seward Glacier and the faults are sketched in their approximate location.

Figure 13. Color scaled velocity magnitude image for the Upper Agassiz Glacier, generated from a correlation done from September 4, 1995 to September 27, 1995. Glacier outline shown in red. See Fig. 2D for regional location.

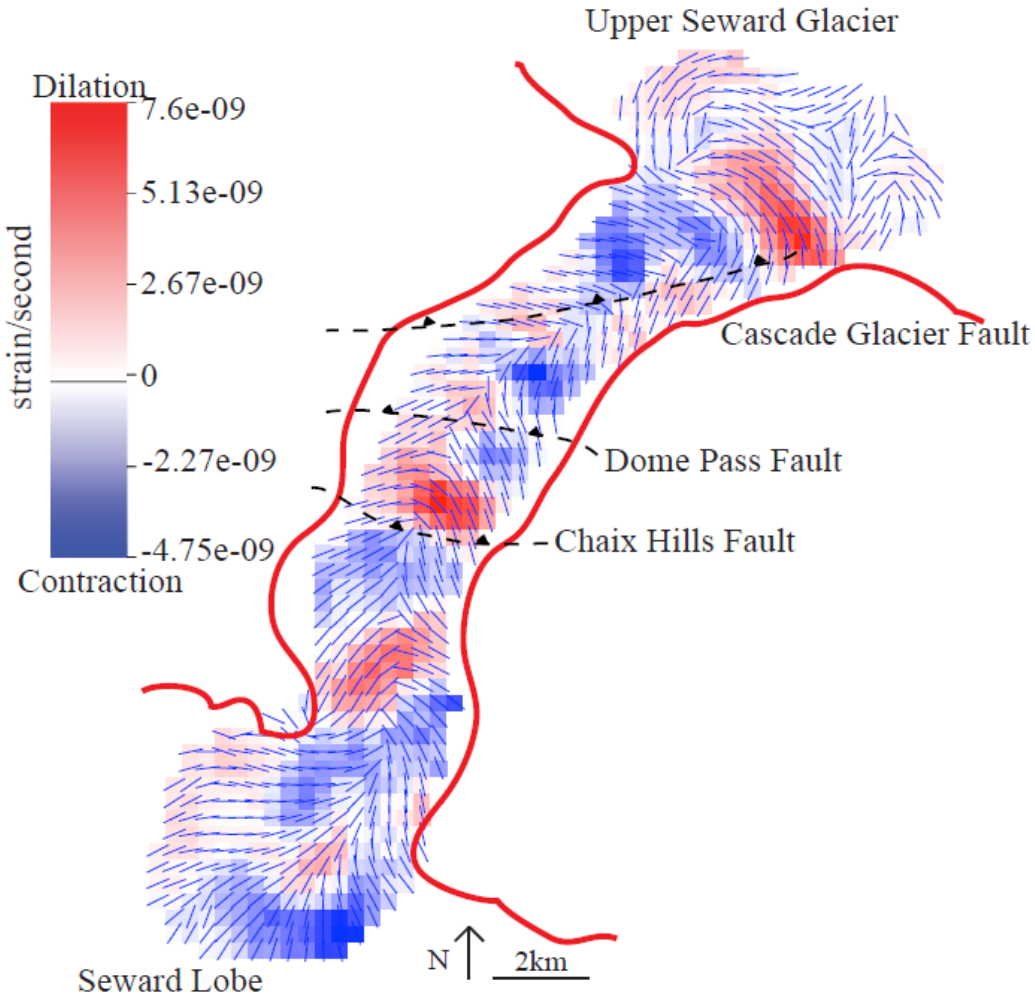
Upper Seward Glacier
Dilation
7.6e-09
5.13e-09
2.67e-09
0
-2.27e-09
-4.75e-09
strain/second
Contraction
Cascade Glacier Fault
Dome Pass Fault
Chaix Hills Fault
Seward Lobe
N
2km

14. Crevasse patterns on the surface of the Agassiz Glacier. Base image is a Landsat 5 Thematic Mapper (band combination 4, 3, 2). Subset images are KH4-Corona satellite images enhanced to highlight crevasses, which are represented by black lines on the surface of the glacier.

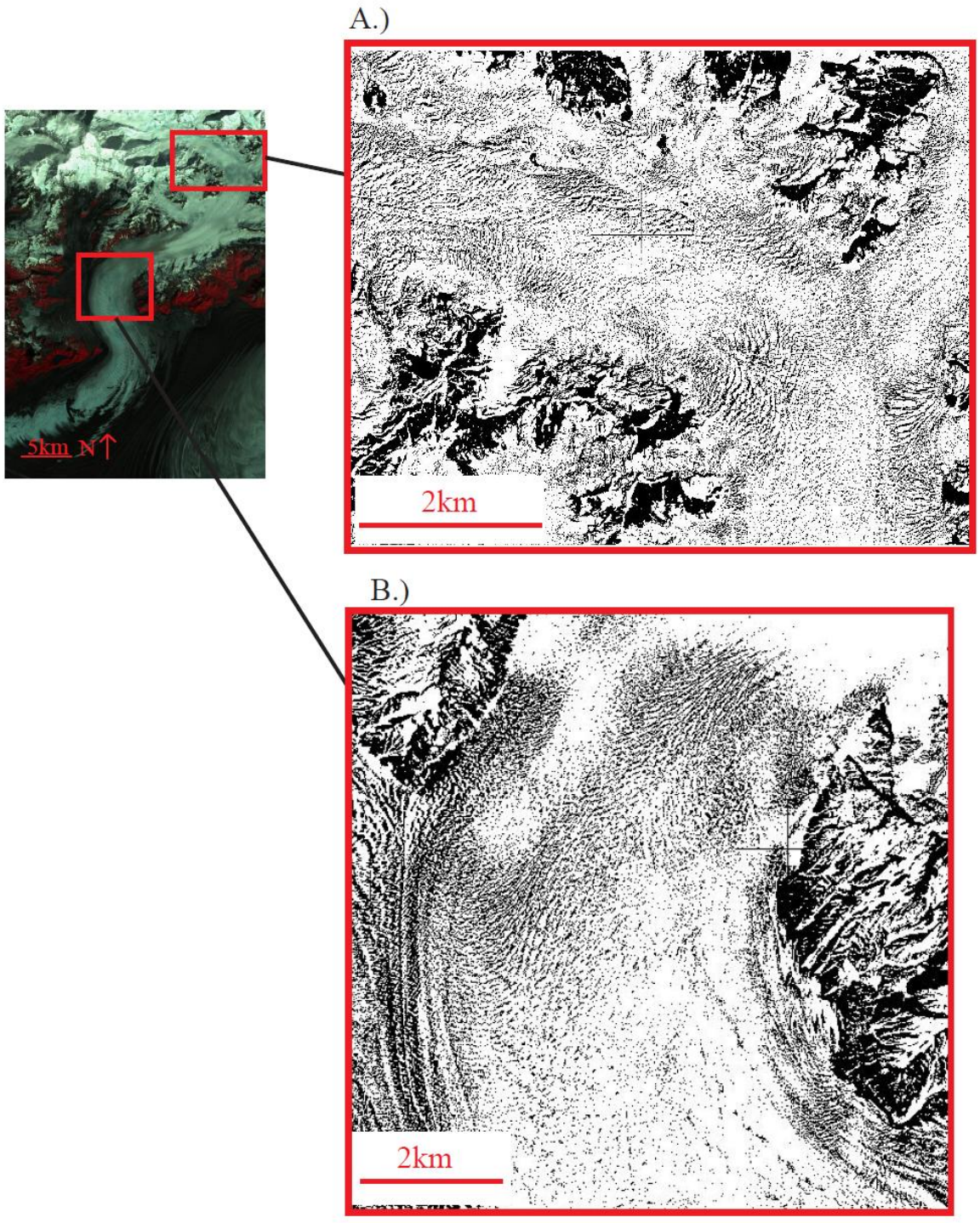
A.)
5km N
2km
B.)
2km

Figure 15. Strain rate map for the Agassiz Glacier generated from the 1995 correlation. Areas in red are undergoing dilation, areas in blue are undergoing contraction and blue lines indicate axis of maximum shortening. Red line represents the outline of the Agassiz Glacier and the faults are sketched in their approximate location.

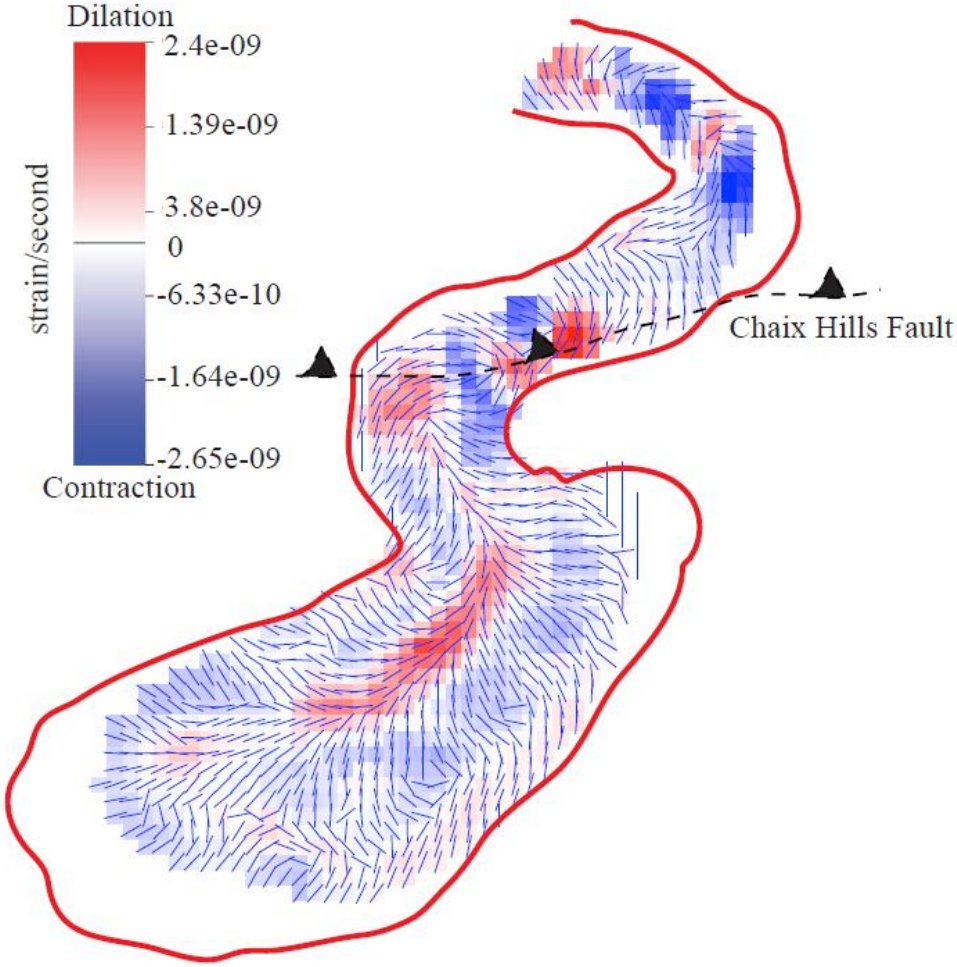
Dilation
2.4e-09
1.39e-09
3.8e-09
0
-6.33e-10
-1.64e-09
-2.65e-09
Contraction
strain/second
Chaix Hills Fault

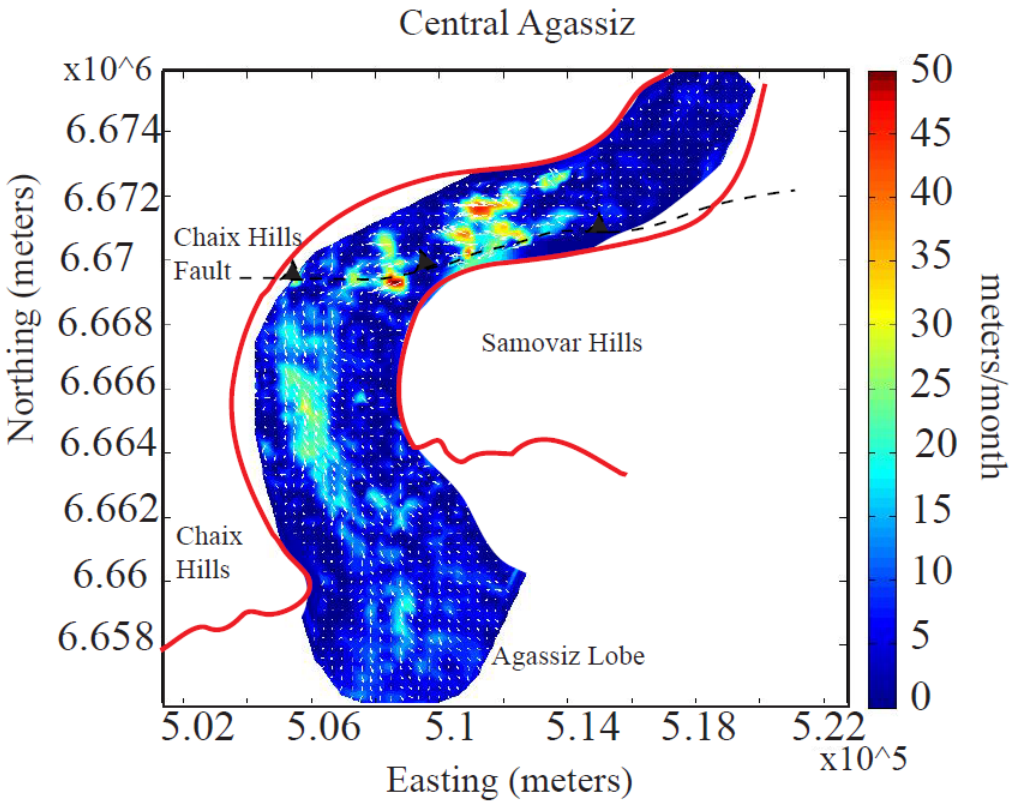

Figure 16. Color scaled velocity magnitude image on the central portion of the Agassiz Glacier generated from correlation done from September 4, 1995 to September 27, 1995. Red line represents the outline of the glacier. See Fig. 2E for regional location.

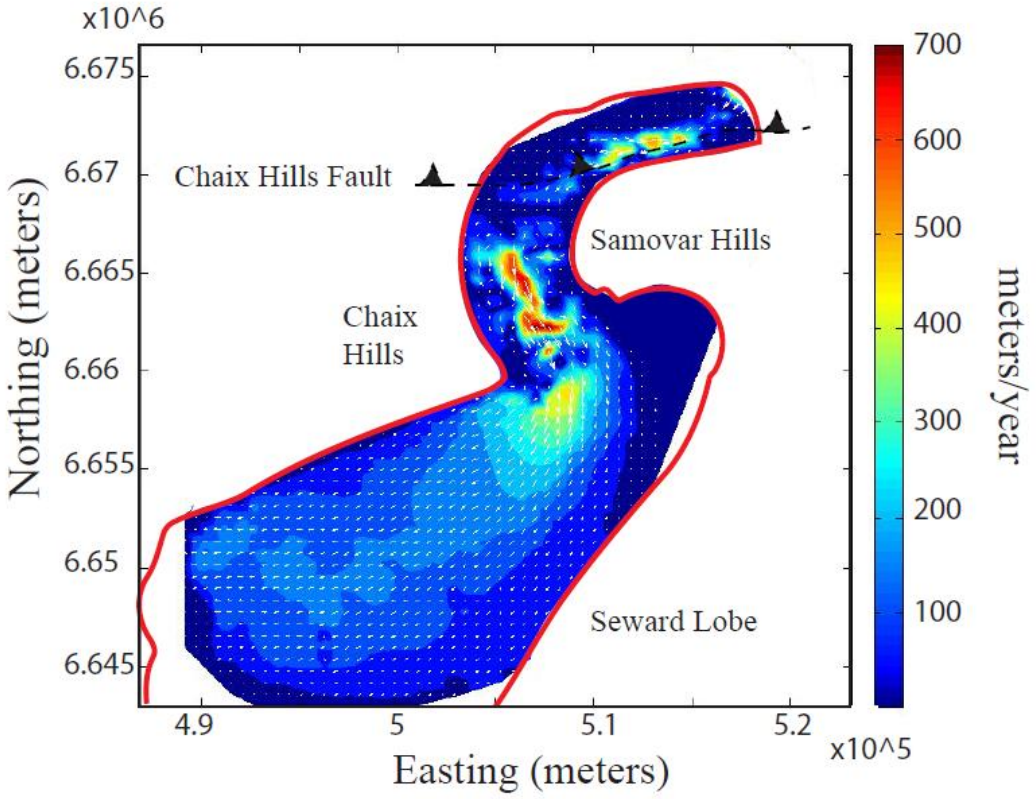

Figure 17. Color scaled image of velocity magnitudes on the Agassiz Glacier generated from correlation done on images between September 11, 1986 and August 29, 1987. Red line represent glacial outline. See Fig. 2 E and F for regional location.

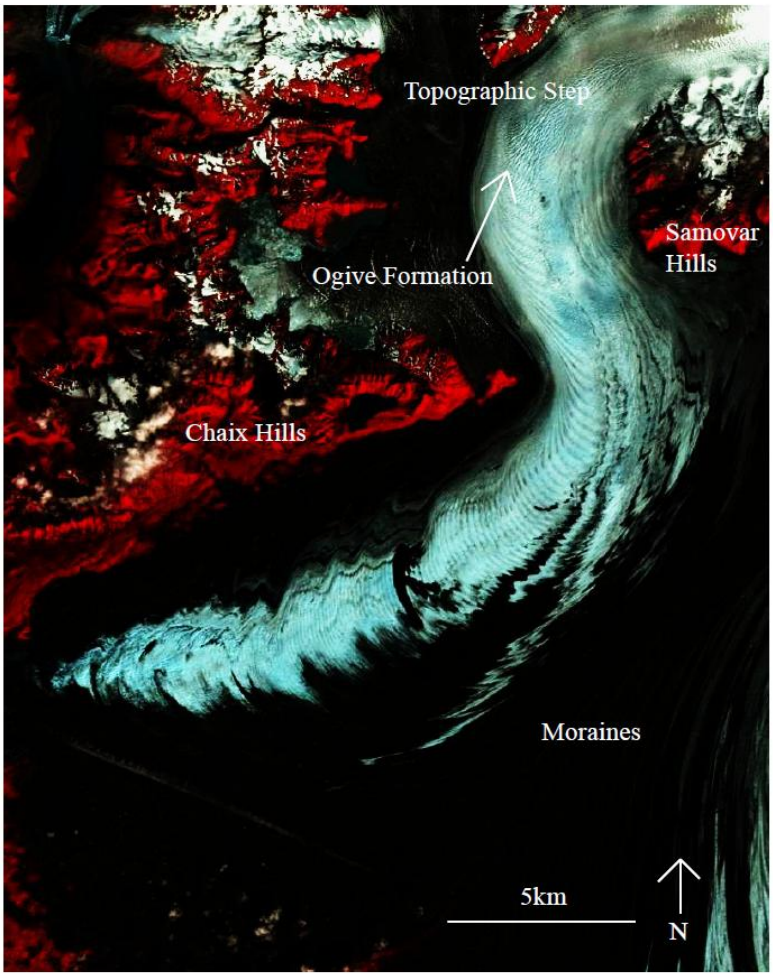

Figure 18. Landsat 5TM image (band combination 4, 3, 2) highlighting ogives on the surface of the Agassiz Glacier, formation of ogives begins after a topographic step on the surface of the glacier.

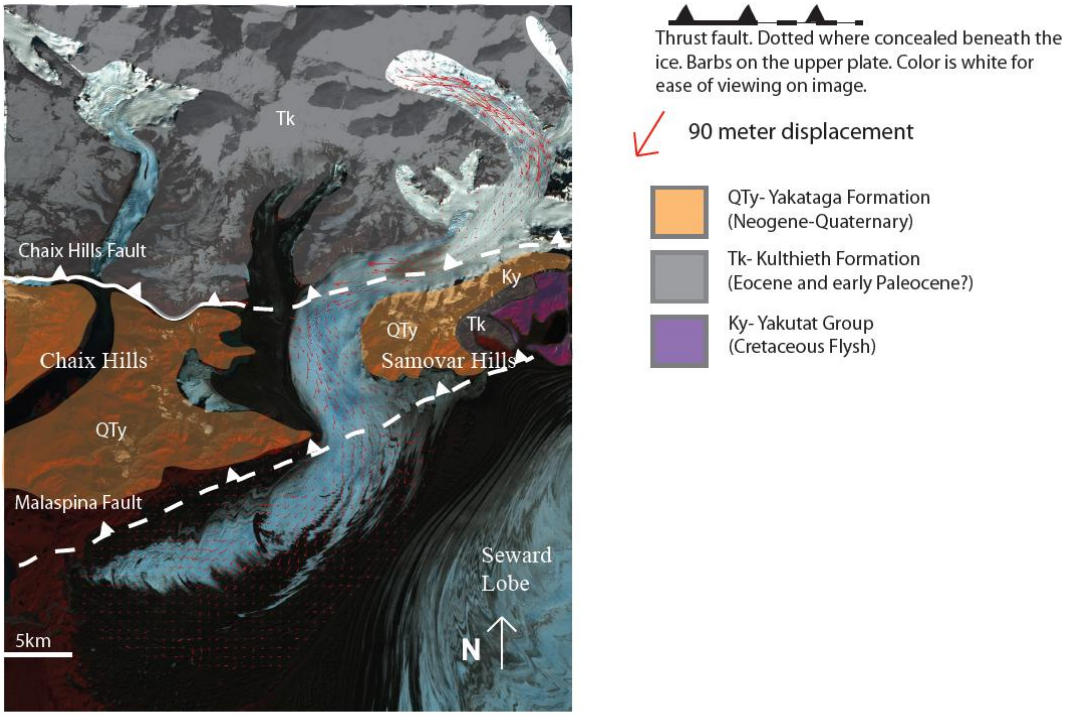

Figure 19. Vectors overlain on a Landsat 5 Thematic Mapper image. The major lithology surrounding the glacier is shown and the geologic structures are inferred beneath the ice.

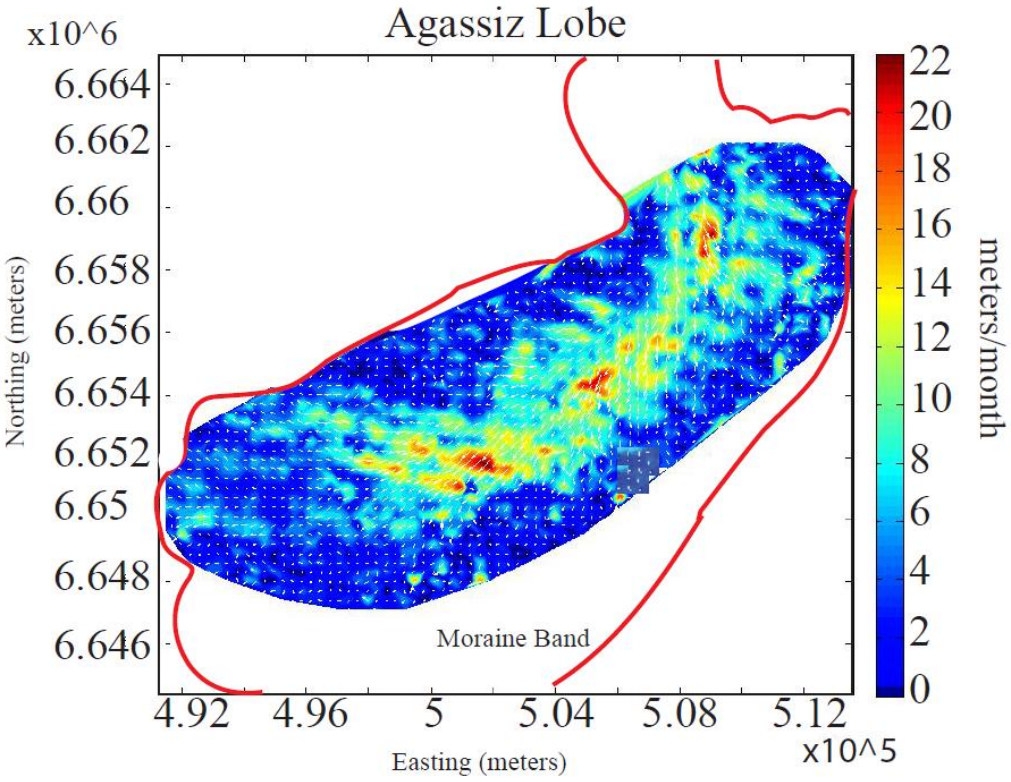

Figure 20. Color scaled image of velocity magnitudes for the Agassiz Lobe generated from a correlation done between September 4, 1995 and September 27, 1995. Red line represents outline of actual glacier. See Fig. 2F for locations.

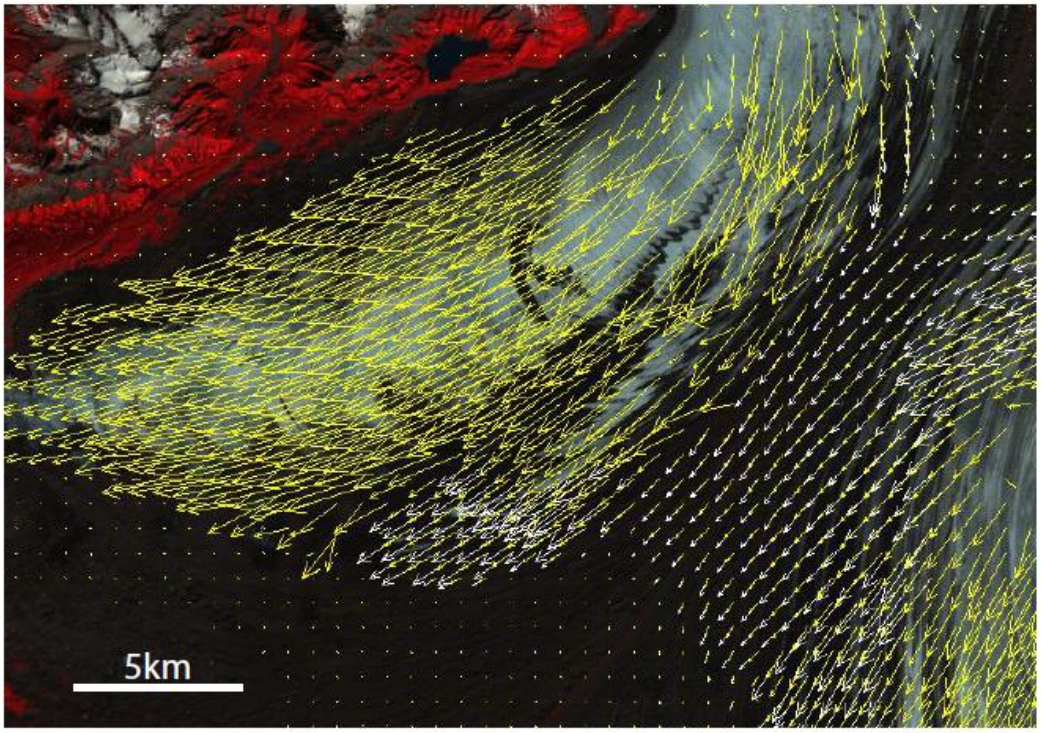

Figure 21. Vector overlain on a Landsat 5 Thematic Mapper image (band combination 4, 3, 2). Yellow vectors generated from movement on the ice between September 11, 1986 and August 29, 1987, white velocity vectors generated from movement on the ice between from July 28, 1999 and Aug 2, 2001 correlation.

Figure 22. Color scaled velocity magnitude image for the Seward Lobe generated from Landsat 5 Thematic Mapper images. A) Velocities from a correlation done between September 11, 1986 to August 29, 1987 B) Velocities from a correlation done between July 28, 1999 to August 2, 2001. The red line represents the outline of the Seward Lobe. See Fig. 2C for location.

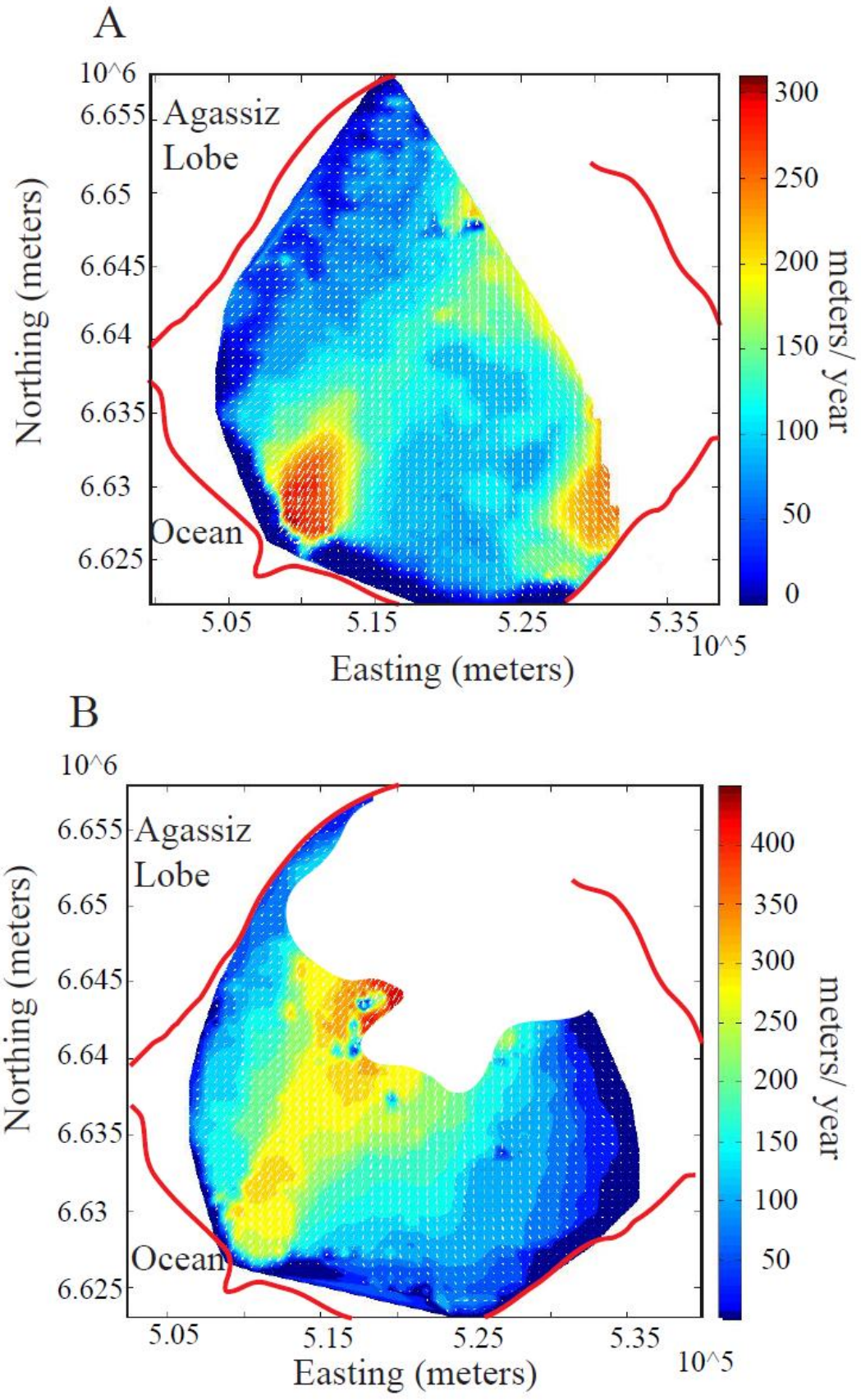
A
10^6
6.655
6.65
6.645
6.64
6.635
6.63
6.625
Northing (meters)
Agassiz
Lobe
Ocean
5.05
5.15
5.25
5.35
10^5
Easting (meters)
300
250
200
150
100
50
0
meters/ year
B
10^6
6.655
6.65
6.645
6.64
6.635
6.63
6.625
Northing (meters)
Agassiz
Lobe
Ocean
5.05
5.15
5.25
5.35
10^5
Easting (meters)
400
350
300
250
200
150
100
50
meters/ year

Figure 23. Topography on the Seward Lobe of the Malaspina Glacier. A) Subglacial topography generated by Conway et al. (2009). Yellow lines are the approximate projection of the subglacial trough between point's c and d on the profile. B) SRTM of the lower half of the Seward Lobe, channel present on the surface corresponds to the location of the tongue of fast flow.

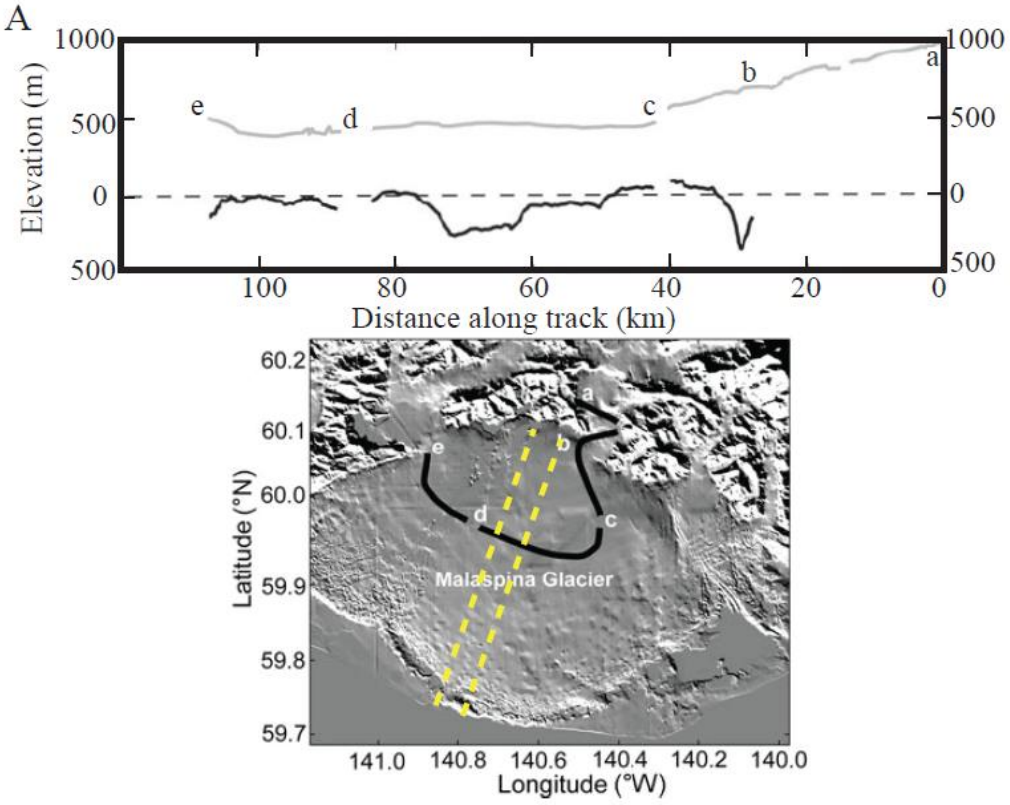
A
Elevation (m)
1000
500
0
500
1000
500
0
500
e
d
c
b
a
100
80
60
40
20
0
Distance along track (km)
60.2
60.1
60.0
59.9
59.8
59.7
Latitude (°N)
a
b
c
d
e
Malaspina Glacier
141.0
140.8
140.6
140.4
140.2
140.0
Longitude (°W)

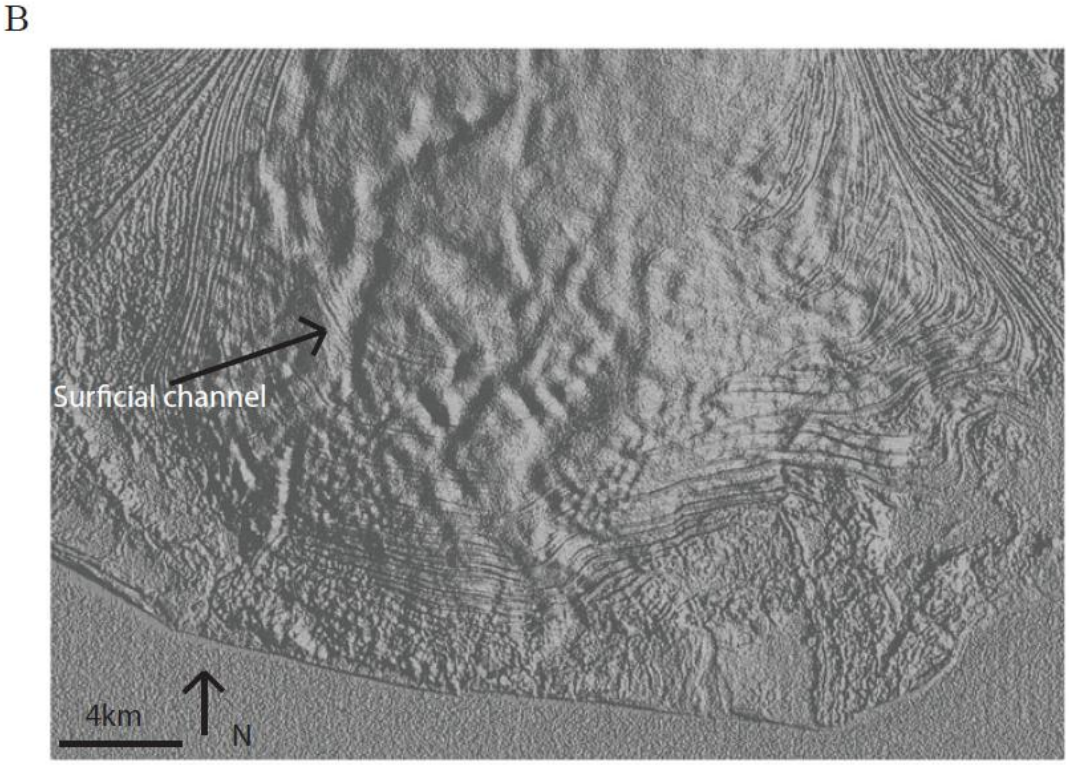
B
Surficial channel
4km
N

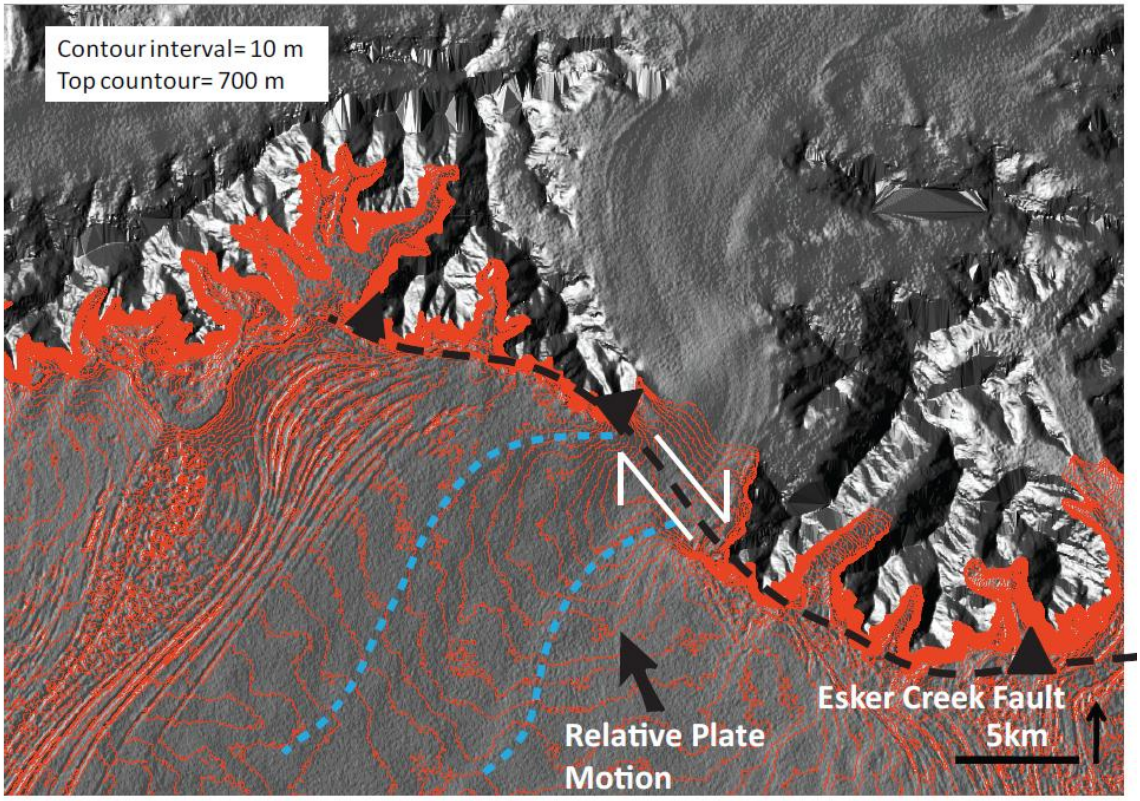

Figure 24. A contoured SRTM image of the transition of ice from the Lower Seward Glacier to the Seward Lobe, with the top contour at 700 m and 10 m contour intervals. The dotted blue line outlines the ridge of elevated ice flowing out the Lower Seward Glacier that is offset to the west.

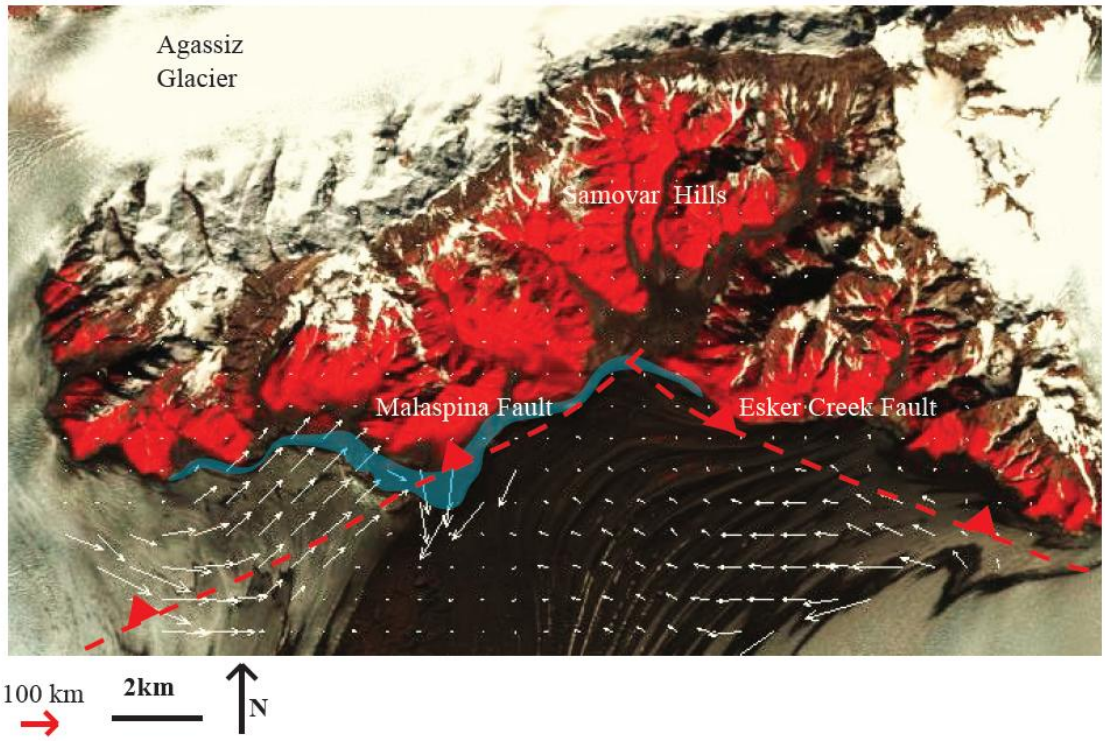

Figure 25. Landsat 5 TM image with COSI-Corr velocity vectors overlain. Oily Lake is a glacial dammed lake that resides in a topographic low in the southern front of the Samovar Hills and is highlighted in blue.

Figure 26. Crevasses patterns around Oily Lake with collapse pits highlighted in blue. The collapse pits are present down the length of the moraine band and can be traced to Yana Stream, a possible discharge point for water drainage from Oily Lake.

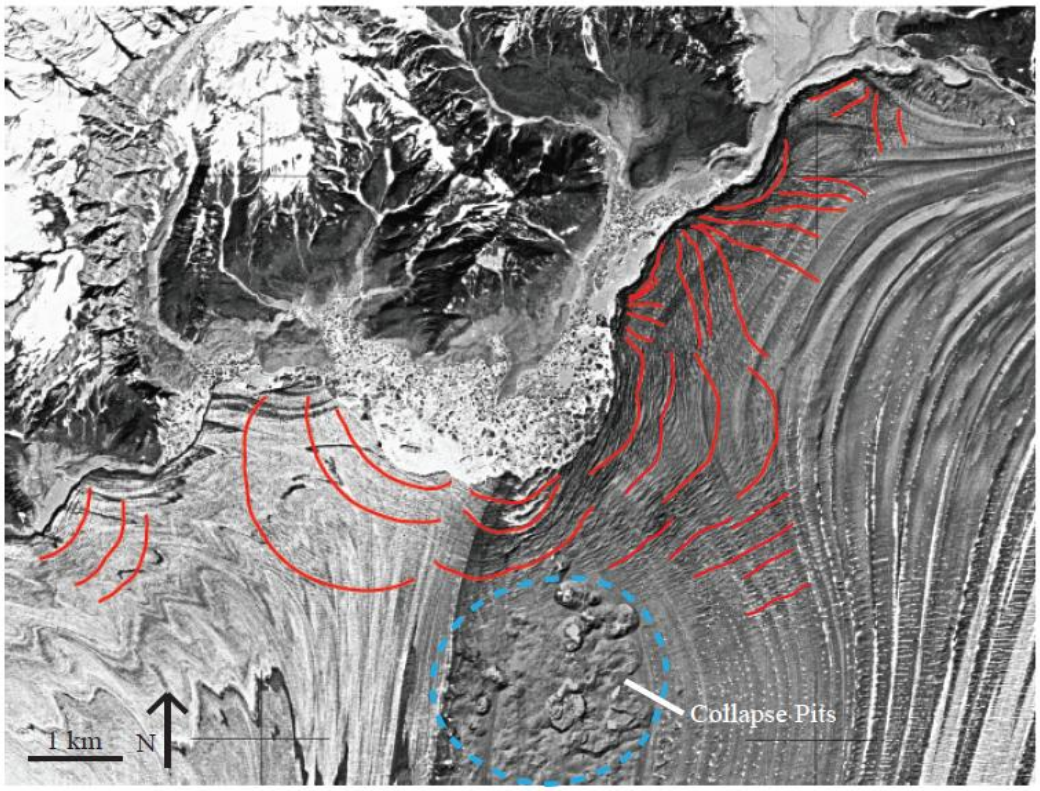
Collapse Pits
1 km
N

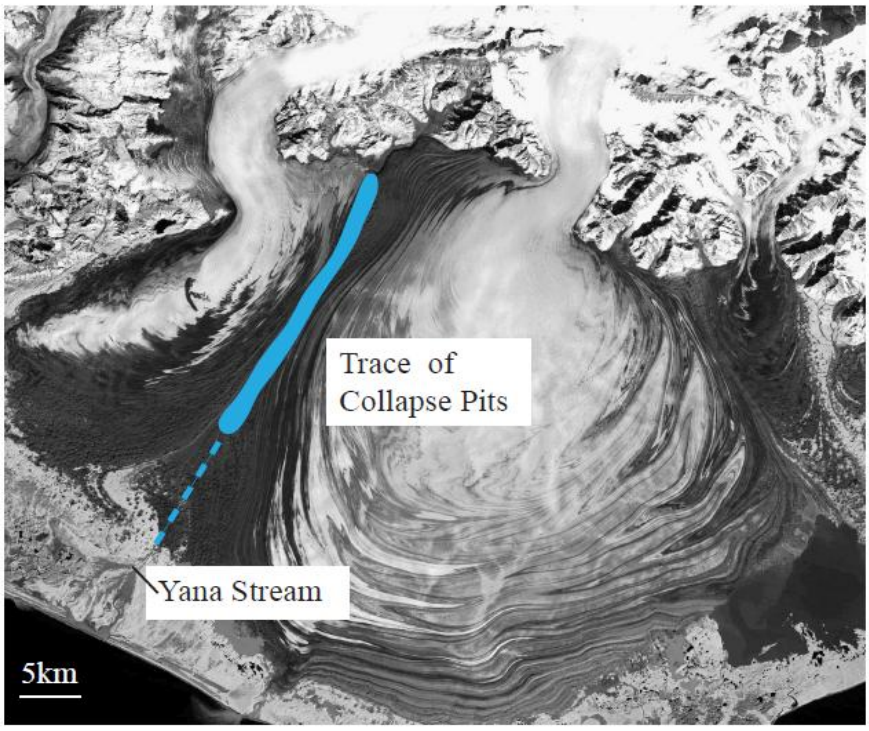
Trace of
Collapse Pits
Yana Stream
5km

DISCUSSION

Affects of Rock Structure on Ice Flow

The ice of the Malaspina Glacier flows over several large geologic structures (Figs. 3 and 4), with known locations and geometries that can be traced beneath the ice. The interaction between these structures and the ice is used to understand how surface topography, flow, and ice structures respond to the underlying geology. The results from this study are subsequently used to predict the nature of structures that lie beneath the glaciers in regions where the underlying geology is not well constrained.

The Upper Seward Glacier; Strike Slip Fault Termination

The Upper Seward Glacier (Fig. 2A) is located at a tectonic juncture between the termination of the Fairweather Transform Fault in the east and Bagley Fault (also referred to as the Contact Fault) (Plakfer, 1987) in the west (Fig. 27). A northwest trending topographic ridge extends across the Upper Seward Glacier at a high angle to the Fairweather and Bagley Fault, and is responsible for subdividing ice flow into two distinct regions on the glacier (Fig. 27). This structure is proposed to be a down to the west normal fault formed from the abrupt termination of the Fairweather Fault (Ford et al., 2003). Coincident with the northwest structure is the Cascade Glacier Fault, a thrust fault that trends toward the northeast and is situated approximately perpendicular to the proposed northwest trending normal fault. The structural configuration of the Upper Seward Glacier illustrates on a large scale, a classic termination of a strike slip fault with

regions of extension (the northwest ridge/ normal fault) and compression (Cascade Glacier Thrust Fault) that are situated orthogonal to each other (Fletcher and Pollard, 1981). This interpretation is supported by the distributions of fault rupturing and aftershocks during the M 7.9 Fairweather Fault earthquake in 1958 (Doser and Rodriguez, 2010). The Fairweather Fault ruptured into the eastern Seward Glacier Basin averaging 4 m of right lateral slip during the earthquake, which was followed by a band of aftershocks that surrounded the termination of the fault and possibly activated the extensional and compressional fault splays beneath the basin. The Cascade Glacier Fault, if reactivated, will tend to close the outlet valley of the glacier, while at the same time provide highly fractured rock and weak 'till' to the base of the glacier to enhance the rate of flow down slope, and also widen the valley by erosion. Therefore, the width of the head of the Lower Seward Glacier may be controlled by the relationship between two competing processes: tectonics (thrust faulting that closes the valley) and erosion (that widens the valley).

Origin of Ice Falls and Their Relation to Thrust Faulting

Topographic steps present on both the Lower Seward Glacier and the central portion of the Agassiz Glacier are associated with the location of underlying thrust faults. The topographic step on the Lower Seward Glacier occurs where the structural duplex of the Dome Pass and Chaix Hills Faults cross beneath the glacier (Fig. 11). Here rocks from the Yakutat Group are faulted over the top of younger rocks of the Poul Creek Formation, which are in turn faulted over Yakataga Formation and Yakutat Group strata in the footwall of the underlying Chaix Hills Fault (Fig. 11). The glacier's surface steepens from an angle of 2º above the step to 6º at the step, and then declines to an angle

of 2º degrees at the base of the step. The steep topography of the icefall corresponds to higher velocities on the surface of the ice (Figs. 9 and 11), transverse crevasses (Fig. 10), and a region of dilatation on the strain rate map (Fig. 12). All these features indicate that the glacier is in extensional flow over the step created by the structural duplex of the Dome Pass and Chaix Hills Fault.

The formation of this step is interpreted as rock cliff retreat where the ice differentially erodes the underlying lithology. The Poul Creek and Yakataga Formation are glacial marine and marine sedimentary rock that are younger, less indurated, and more easily eroded than the metamorphosed flysch of the Yakutat Group. As ice flows across the structural duplex, the faulted and fractured rocks of the Poul Creek and Yakataga Formation erode preferentially, presumably by ice plucking, relative to the more indurated rock of the Yakutat Group. The difference in rates of erosion presumably undermines the more indurated rock of the Yakutat Group, which then collapses beneath the ice fall, maintaining a steep slope (Fig. 11).

The topographic steps on the central portion of the Agassiz Glacier begin at a similar geologic transition that is found on the Lower Seward. The steps are located near the southwestern end of the Samovar Hills where the Chaix Hills Fault is traced beneath the glacier (Figs. 4 and 6). Here rocks of the Kultieth Formation are faulted over younger rocks of the Yakataga Formation. Above the step, the surface of the glacier slopes at 1º-2º angle where ice flows over the Kultieth Formation, and increases to a 4º angle where the ice flows over the Chaix Hills Fault at the topographic step and continues to flow over the Yakataga Formation. The most prominent feature associated with this step is the intense crevassing present on the surface of the glacier and the initiation of ogives, alternating

bands of light and dark ice that form on the surface of a glacier below an ice fall (Fig.18).

The topographic steps on the surface of the Agassiz Glacier most likely are formed by differential erosion of the underlying rocks. Rocks of the Yakataga Formation are less indurated and more easily eroded than the rocks of the Kultieth Formation; this combined with faulting on the Chaix Hills Fault and subsequent fracturing of rock around the fault surface allows the glacier to preferentially erode into this contact, and steepen the basal slope.

The formation of ice falls on the surface of the Lower Seward Glacier and the Agassiz Glacier are related to the underlying geology. This implies that as glaciers flow over geologic structures that extend beneath the ice and juxtapose lithologies of different competence, a topographic step develops because of differential erosion into the fault zone and underlying rocks. In both examples, topographic steps form where ice has eroded weaker, less indurated rocks and glacial quarrying occurred at faster rates than on the surrounding, more indurated rocks.

Ice Flow Parallel to Faults

The upper section of the Lower Seward Glacier and the central section of the Agassiz Glacier provide the opportunity to explore the dynamics of ice flow where glaciers are confined to valleys that are eroded along major faults (Fig. 4). This is an important structural setting for ice flow, because in many mountain belts, the most pronounced lineaments in the landscape occur where glaciers have previously excavated deep troughs along fault zones that extend for tens of kilometers.

The Cascade Glacier thrust fault is located beneath the upper region of the Lower Seward Glacier, where metamorphosed rocks of the Yakutat Group are juxtaposed on

either side of the fault (Fig. 4). The slope of the glacier steepens to an angle of 6º where ice flows into the head of the Lower Seward Glacier, and then decreases to a slope of 2 º where the ice flows down slope over the trace of the thrust fault. The change in slope is accompanied by a change in ice velocity (Fig. 9). Ice in the main body of the Lower Seward Glacier flows at 10-20 m/month but velocities increase to 40-60 m/month over the topographic step at the head of the Lower Seward Glacier and along the trace of the Cascade Glacier Thrust Fault. Strain rate in this region shows dilation along the trace of the fault, which indicates that the ice is in extensional flow above the underlying fault.

North of the topographic steps on the central portion of the Agassiz Glacier, the Chaix Hills Fault trends parallel to the direction of ice flow (Fig. 4). Velocities on the main body of the glacier increase from 10-15 m/month, to 20-40 m/month along the trace of the fault (Figs. 16 and 17). Dilation on the strain rate map also coincides with the region of increased flow velocity above the Chaix Hills Fault (Fig. 15).

Rock along these contacts are likely weaker and fractured from faulting; quarrying along the fault trace would be easier than on that of surrounding less fractured rock. Hallet et al. (1996) proposed that the spacing and growth of fractures controls the rate of quarrying. Where fractures are closely spaced, glacial quarrying is efficient, in contrast to where the rock is massive with a few fractures and quarrying is ineffective. The surface slopes in these regions do not increase significantly along the trace of the faults, further implying that the rheology of the basal deposits is responsible for the

increased rate of flow. The weaker material may be water saturated till formed from plucking and abrasion of the comminuted fault rock (Boulton and Hindmarsh, 1987). The faster ice velocities are likely correlated to deformation of the underlying till.

Interpretation of Flow Patterns

Fault Propagation Fold under the Agassiz

The Agassiz Glacier flows across the large fault propagation fold formed by the Malaspina Fault where it exits the mountain front and flows towards the west onto the piedmont . The surface slope is 4º as the ice flows out of the mountain front decreasing to ~1º ice moves over the piedmont (Fig. 6). Ice velocity over the step ranges from 300-600 m/year (Fig. 17). The topographic step on the ice surface occurs where the Yakataga Formation is folded above the Malaspina Fault, forming a large fault propagation anticline with a gentle north dipping back limb. East of the Agassiz Glacier, a large anticline plunges towards the west in the upper plate of the Malaspina Fault where it is exposed in the Samovar Hills (Fig. 28). Bruhn et al. (2004) interpreted this structure as an older foreland fold that has been uplifted, exhumed by erosion, and tilted towards the west in the hanging wall of the Malaspina Fault (Fig. 29). The exposures in the Samovar Hills provide a down plunge view of the fault propagation fold across which the Agassiz Glacier flows (Fig. 28). Farther west, this fold disappears beneath the Chaix Hills and continues offshore into the Pamplona Zone where it has been imaged by seismic reflection profiling (Fig. 29) (Worthington et al., 2010).

The topographic steps in the glacier are an example of glacial erosion across the back limb and hinge zone of a fault propagation fold. Three alternative models for the formation of the step are sketched in Figure 30, with the preferred model illustrated on

part 3 of the figure. The alternative models are 1) erosion across the exhumed tip of the Malaspina Fault where the faulted and fracture rocks are quarried out preferentially with respect to the surrounding rock; 2) differential erosion of the beds on the overturned limb forming a topographic step where the base of the glaciers extends across the steeply dipping beds; 3) differential erosion by plucking that removes rock by slip and quarrying along bedding surfaces in the gentle west dipping back limb of the fold. This latter scenario is preferred because the topographic step on the surface of the glacier is bounded on both sides by gently west dipping bedrock and plucking presumably results in a stair case geometry within the bedrock that forms the topographic step and icefall on the surface of the glacier. The steps associated with gently dipping bedrock surfaces are a common geomorphic feature observed in the floors of alpine glacier valleys following retreat of the ice (Hooke, 1991). Also the depth to the base of the glacier (~500 m) measured by Conway et al. (2009) is too shallow for interception of the Malaspina Fault at the base of the glacier, which was penetrated at a depth of 2500 m in the Chaix Hills #1A well (Plafker et al., 1975). Ice on the piedmont is, however, most likely flowing over the steeply dipping forelimb of the fault propagation fold.

Esker Creek Fault: Evidence for Dextral Shearing

The ice at the base of the Lower Seward Glacier is deflected towards the west where it crosses the Esker Creek Fault, and continues to the south beneath the Malaspina Glacier (Fig. 24). The amount of lateral offset is ~1-2 km, and indicates right lateral shearing in addition to reverse slip displacement on the north dipping Esker Creek Fault as proposed by Plafker and Thatcher (2008). Recognizing this lateral component of fault offset is important for several reasons. 1) The Esker Creek Fault ruptured during the M

8.1 earthquake on Sept. 10, 1899, creating the greatest measured cosiesmic uplift during an historical earthquake (Tarr and Martin, 1912). Cosiesmic slip on the Esker Creek Fault uplifted the coast in upper Yakutat Bay by as much as 14 m. 2) A significant component of lateral shearing on the Esker Creek Fault is predicted given the relative motion of the Yakutat microplate with respect to the Alaskan plate margin in this area. The evidence for 1 km of dextral offset therefore confirms the general sense of motion and fault slip predicted by geodetic surveying (Elliott et al., 2010; J. Elliott, personal communication, 2011). 3) This offset may further underscore how the structures of the Fairweather Transform Fault and Aleutian Megathrust are currently linking together beneath the Malaspina Glacier.

Dextral shearing along the mountain front where the fault lies buried beneath the glacier provides a speculative, but plausible, explanation for a narrow trough at the base of the glacier that is observed on the ice penetrating radar profile published by Conway et al. (2009) (Fig. 23a). A linear fault trace that erodes to form a deep trough is common along faults where there is a significant component of lateral motion. In contrast, dip slip faults, and especially thrust faults, create a cuspate mountain front and sinuous fault zone where the moderate or gently dipping fault intersects the Earth's surface. Dextral shearing along the Esker Creek Fault may therefore control the geometry and even the position of the mouth of the Lower Seward Glacier where ice debauches onto the head of the Malaspina Glacier. The mountain front is offset to the north approximately 1 km at the base of the Lower Seward Glacier, as though the glacier exits the range front in a small pull apart basin formed within a right lateral shear zone (Fig. 24).

Oily Lake - Formation and Drainage

Oily Lake is located where the Malaspina and Esker Creek Faults intersect and form a structurally controlled groin in the Samovar Hills. Elevations on the surface of the glacier decrease towards Oily Lake, and tongues of ice flow towards the lake from the mouths of the Lower Seward Glacier and Agassiz Glacier (Fig. 25). The subglacier trough of the Esker Creek Fault presumably continues to the west along the mountain front towards the Samovar Hills where it intersects the Malaspina Fault. Oily Lake is then located in the depression formed by erosion of these two faults.

Understanding the interactions between the lake and glacier are important because of the potential for outburst flooding at the terminus of the Malaspina glacier, and possible link of outburst flooding to surging of the glacier. Oily lake shows evidence of extending subglacially from the radial crevasses that extend approximately .5-1 km beyond the ice/water boundary of the lake. Another feature that suggests that the ice extends sub glacially are the collapse pits on the surface of the glacier that extend southward from the lake along the band of moraines leading to Yana stream at the terminus of the glacier (Fig. 26). The sizes of the pits vary from tens of meters to hundreds of meters and suggest the collapse of englacial conduits that drain water from Oil Lake. Ice flow paths down the moraines, observed from the correlation results, show that the ice flows south subparallel with the trace of the collapse pits (Fig. 26). Water from potential outburst floods would presumably mimic the current flow path of ice and trace of the collapse pits observed on the surface of the ice. The most likely discharge point for outburst flood would occur in the vicinity of Yana stream at the terminus of the moraine band between the Seward and Agassiz Lobe of the glacier.

Flow on the Agassiz Lobe

Directions of ice flow on the Agassiz Lobe and adjacent moraine band diverge on the piedmont, with ice on the Agassiz Lobe moving towards the west and ice in the moraine band flowing south (Fig. 21). Three possible explanations may account for the westward deflection of flow seen on the Agassiz Lobe. 1) Ice from the Seward Lobe spreads out onto the piedmont and pushes the ice in the Agassiz Lobe towards the west. If this were the case, ice in the moraine band would show a similar westward deflection; flow in the moraine band does not appear to be diverted towards the west but trends south towards the coast (Fig. 21). 2) Ice is flowing parallel to bedding of the steep forelimb of the fault propagation fold that underlines the Agassiz lobe. 3) Flow is deflected toward the west by uplift on an incipient fault that is oriented subparallel to but located to the east of the Malaspina. Evidence for faulting beneath this part of the glacier includes several aftershocks from the M 7.3 Saint Elias earthquake (Estabrook et al., 1992). Also there is evidence for uplift of the coast just east of the moraine band where a series of beach berms appear to have been uplifted in the hanging wall of a thrust fault. Trees logged from this site show growth of about 100 years dating back to about 1900-1904. Uplift of the beach berms may have occurred during the great earthquakes of 1899 that occurred in the region of the Malaspina Glacier (R.L. Bruhn, personal communication, 2011).

COSI-Corr- Relevance to Glacial Monitoring

COSI-Corr has proven to be reliable software for accurately tracking and monitoring ice flow on glaciers (Leprince et al., 2007a, b; Scherler et al., 2008). Flow fields generated for the Malaspina Glacier System illustrate the ability of COSI-Corr to

track subpixel ice motion over a variety of timescales and flow conditions. The success of feature tracking can be hindered by the correlation routine because it does not discriminate between the image sensor, spectrum, or timescale; thus miscorrelations can be common if the user input parameters are unsuitable for the images that are being analyzed. When running a correlation on glacial images, a number of important points must be kept in mind to generate accurate results.

First, the images that are being compared should have similar snow cover. Images that contain vastly different snow cover characteristics, as in images from summer and winter, are difficult to correlate as features on the surface of the glacier are significantly different in "snow" and "no snow" conditions (Scherler et al., 2008). Images from the same season usually work well as surface features are likely to be similar and easier to track. For the Malaspina Glacier System, the best results were generated from summer season where snow cover is diminished and surface features (folds, crevasses, and debris) are clearly visible.

Second, cloud cover over the glacier needs to be low. Cloud cover is a major restriction when using optical satellite imagery, if clouds are present over the glacier, accurate correlations cannot be made. Thin partly transparent clouds may not pose a significant problem to correlation (Scherler et al., 2008), so scenes with some cloud cover can be used. Also, scenes with a large percentage of cloud cover can be used as long as the area of interest is not covered by clouds.

Third, some knowledge is needed of the actual flow conditions on the surface of the glacier to determine the parameters used in COSI-Corr and to analyze the resulting flow field. General trends of glacial flow and rates can be inferred from visual inspection

of the images. COSI-Corr uses an unbiased processor and miscorrelations are common in areas of intense crevassing, shadowing, pooling water, and differing snow cover. Miscorrelations are characterized by vectors that point up glacier, opposite to flow, or vectors that greatly exceed reasonable rates of flow. These vectors can be removed or edited as discussed previously. For the Malaspina Glacier, the general direction of glacial ice motion is seen when flicking between two images. Manual measurements were made in several areas of the glacier to determine a general flow rate, which were then compared to the results generated in COSI-Corr. By adjusting the parameters within COSI-Corr's correlation routine, accurate measurements of velocity could be determined for the majority of the glacier surface. This is illustrated in the results of the Seward Lobe; correlations done in COSI-Corr show surface velocities on the Seward Glacier Lobe in the range of .2 to .82 m/day (correlation from 1986 to 1987) and .2 to 1.2 m/day (correlation from 1999-2001); Sharp (1958) manually measured velocities in the range of .5 to 1 m/day in the same region, velocities that compare to this study's results.

Fourth, the velocity of the glacier and temporal separation of images can complicate the correlation procedure. When velocities on the glacier are high, shorter time spans between images produce better correlations. Conversely slower velocities correlate better over longer time spans. This is illustrated on the Lower Seward Glacier and Seward Lobe. Images compared over a month timescale were able to accurately track velocities on the Lower Seward Glacier, while the Seward Glacier Lobe contained predominately miscorrelated velocities. Over longer time spans of a year to 2 years accurate velocities for the Seward Lobe were calculated but ice motion was too rapid on the Lower Seward Glacier to be tracked over the longer time span. Several correlations

over differing time spans were needed to accurately track motion over the entire glacier system.

Fifth, the search window size must be scaled to the amount of motion on the glacier. If search windows are too large or small, the correlations will be inaccurate. In general, longer time spans between images need larger window sizes to track ice displacement and vice versa for shorter time spans. The longer the temporal span between images, the greater amount of ice displacement and larger search area needed in COSI-Corr to accurately track ice motion. As ice movement can be variable on the surface of the glacier, the scaling option in the frequential correlator is useful to track both large and small scale movement on the glacier. To determine what window size(s) would be best to correlate on the Malaspina Glacier, manually measured ice motion was used to determine an upper limit for the window size. If correlations were inaccurate, with the majority of results miscorrelated, window sizes were adjusted to larger or smaller size until an accurate field was calculated. To generate the best results for the Lower Seward Glacier and Agassiz Glacier, multiscaling window sizes of 32x32 pixels scaled down to 4x4 pixels were used; for year correlations on the piedmont, multiscaling windows of 64x64 pixels scaled down to windows of 4x4 were used.

General Observations on Glacier Structure and Hydrology

Ogives and Surface Velocity

Ogives on the surface of the Agassiz Glacier are unique features found nowhere else on the surface of Malaspina Glacier system (Fig. 18). Ogives are recognized by a light and dark banding that have a convex down glacier shape and form below an ice fall where the glacier surface is fractured by multiple sets of crevasses (King and Lewis,

1961). The dark band forms in the summer when ablation is at its maximum and snow cover at a minimum. Dirt and dust transported from snow-free slopes are deposited within the crevassed region to create a dark band of ice with high dirt content. The lighter band is formed during the winter when ablation is low and snow accumulation is high; little dirt is transported onto the ice because adjacent slopes are covered with snow. This process creates the white band of the ogive (Allen et al., 1960). The difference in albedo between the light and dark band can lead to wavy topography on the surface of the glacier because the dark bands ablates at a faster rate and forms a topographic low. Dirt can accumulate within this low and further accentuate the dark band (King and Lewis, 1961).

Ogives on the central portion of the Agassiz form below the topographic step on the surface of the glacier near the southern tip of the Samovar Hills and location of Chaix Hills Fault trace (Figs. 4 and 6). In this region, the surface of the glacier is marked by heavy crevassing (Fig. 14). The annual bands (light and dark) are on average 400-500 m wide with white bands thicker, averaging 300 to 350 m in width and dark bands averaging 100-150 m in width. Towards the outer margins of the glacier the ogives narrow to 100-200 m thick. The change in width is a common characteristic of ogives and correlates with the decrease in velocity as you move from the centerline of the glacier to the margins where ice velocity slows due to friction along the glacier walls. Annual ogive thickness is linked to glacier motion and should reflect yearly movement on the ice. A correlation done on the Agassiz from 1986 to 1987 calculated velocities that ranged from 100 m per year on the margins and up to 600 m down the central portion of the glacier (Fig. 17). This suggests that the ogives on the Agassiz Glacier are annual features and

roughly estimate ice motion. Farther down glacier on the piedmont, the velocities slow and ogives become thin as the ice contracts. The ogives disappear 3 to 4 km before the terminus of the glacier and are presumably removed by ablation.

Strain on the surface of the Agassiz Glacier shows a pattern of dilation around the centerline of the glacier surrounded by zones of contraction as you move toward the margins of the glacier (Fig. 15), with the shape of the ogives mimicking the strain present on the glacier. The central portions of the ogives are extended down where the glacier is undergoing dilation. Near the margins, strain shows contraction and the ogives tend to curve up towards the valley wall because of increased shear strain (Fig. 18).

Basal Hydrology Relation to Glacial Flow

An important note to make when correlating glacier surface features and flow patterns to the basal topography is that surface flow features may not correlate directly with the spatial distribution of topography beneath the glacier. Variations in surface flow can be influenced by the underlying rheology of basement cover and cause spatial variations of surface flow from the resistance to basal sliding at the glacier bed. Also as pore water within the glacier increases, higher water pressures at the base of the glacier can lead to deformation of underlying till and cause glacial sliding; this translates to acceleration of flow on the surface of the glacier (Fountain and Walder, 1998).

The Malaspina Glacier System is a temperate glacier that is near the pressure melting point and has a high water table. The water within the Malaspina Glacier moves through a system of internal conduits and discharges at ice marginal fountains at the head of outwash fans (Gustavson and Boothroyd, 1987). During the spring and early summer, melt causes the water flux to increase and leads to periods of rapid flow, most likely from

basal sliding and deformation of the underlying till. This can be problematic when analyzing flow features on a small scale, but as most flow features on the Malaspina Glacier are a kilometer or larger, variations in rheology most likely mimic the underlying topography. For example, fast flow will occur where the deformable till is thick in subglacial troughs and flow would be decreased over ridges where glacial till is thinner (Bruhn et al., 2010). The tongue of fast flow seen on the Seward Lobe (Fig. 22) is linked to a subglacial trough which is presumably filled with deformable sediment as evidenced from sediment laden water that discharges at the terminus of the glacier.

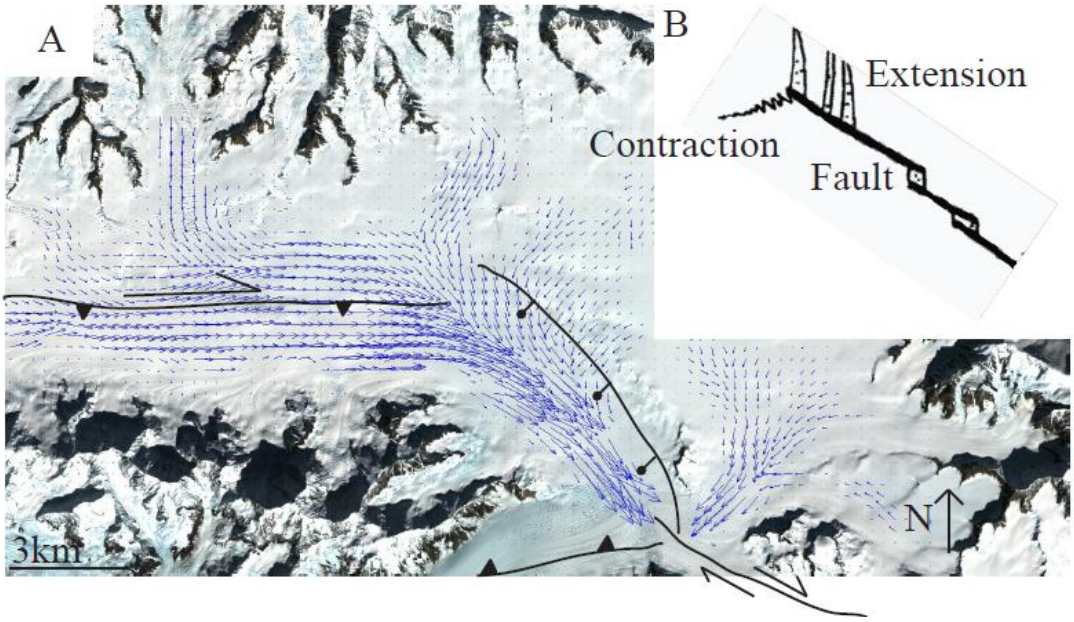

Figure 27 Landsat Thematic Mapper image (band combination 3,2,1) , with velocity vectors overlain. A.) Proposed structural model for the Upper Seward Glacier, illustrating the structures involved in the termination of the Fairweather Fault B) Model of structures that form at a fault termination from Fletcher and Pollard, 1981. Configuration of actual faults in the Upper Seward compares to this model.

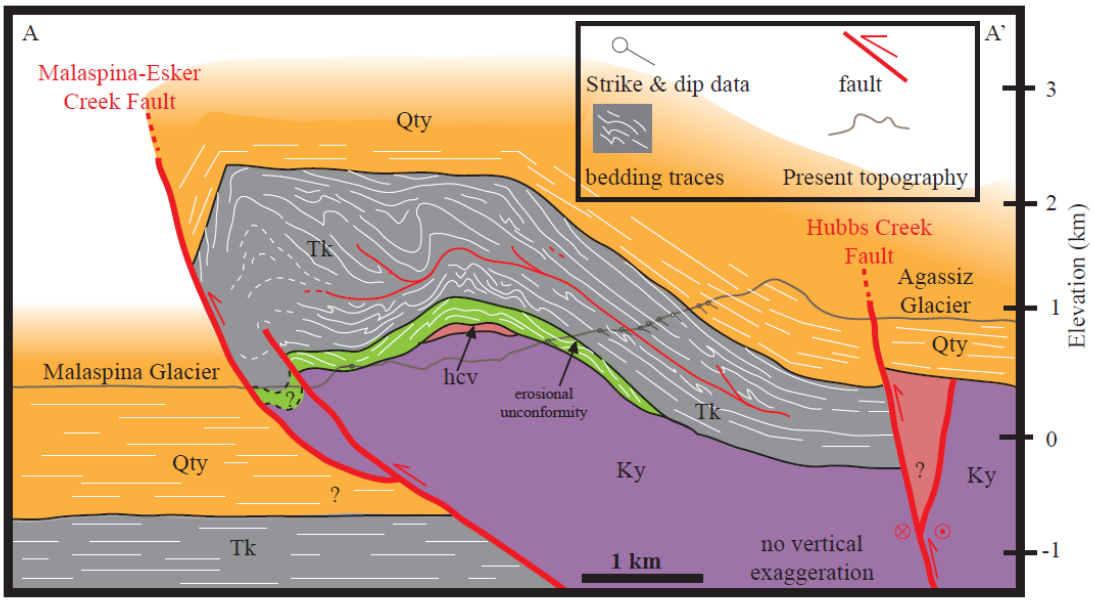

Figure 28. Cross section A-A', a large box fold that plunges to the west and is located in the Samovar Hills. See Fig. 4 for location. Figure modified from Chapman et al., in press.

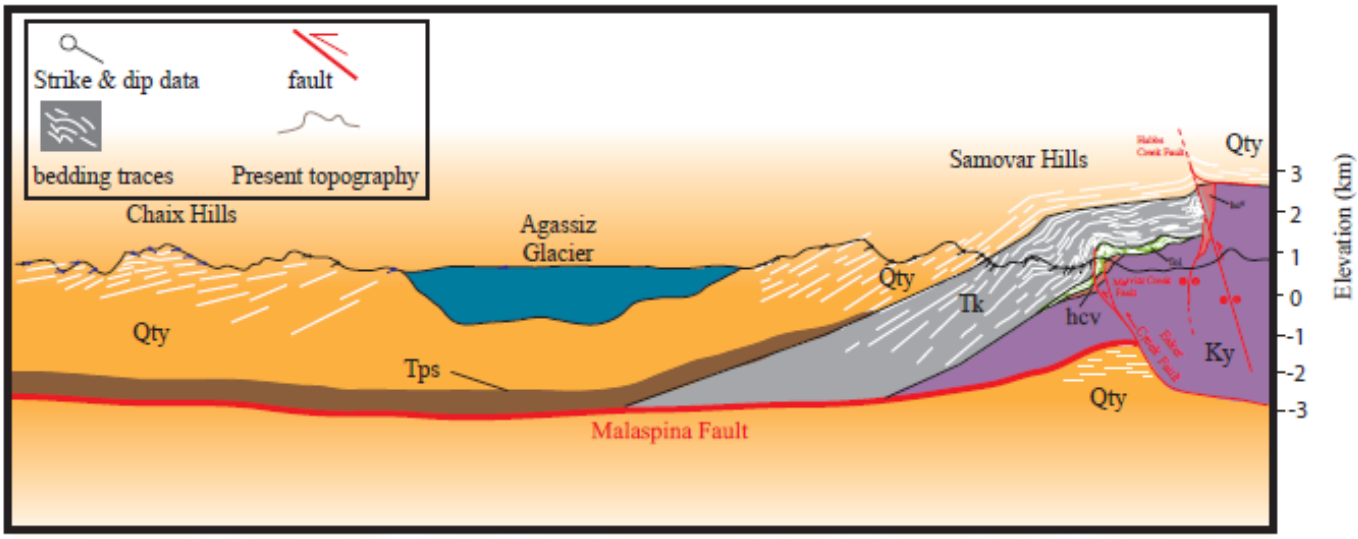

Figure 29. Cross section B-B', the structure of the Samovar and Chaix Hills. See Fig. 4 for location. Figure modified from Chapman et al., in press.

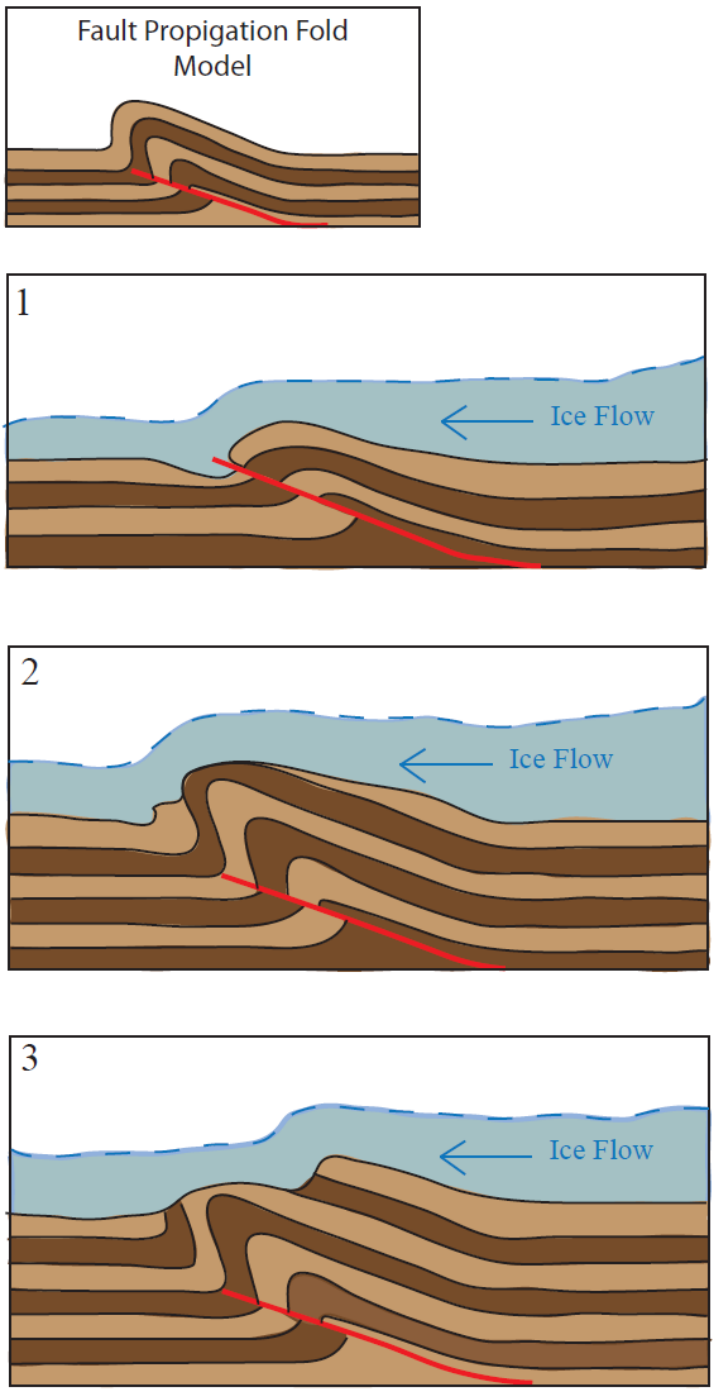

Figure 30. Geologic cartoon cross sections of a fault propagation fold. Three erosion models for the Agassiz Glacier are shown. The lighter rock layer erodes preferentially to that of the darker rock layer.

CONCLUSIONS

Results from this study show that optical feature tracking of ice motion on the alpine and piedmont lobes of the Malaspina Glacier System provides information on the velocity fields averaged over two discrete periods of time, ranging from 1 month for scenes acquired during a summer season to about 1 to 2 years for scenes acquired during two different summers. The resolution in ice displacement using the image cross correlation algorithm implemented in COSI-Corr software for this study is about 1/15 of a pixel, or 2 m. Measured velocities range from 10-30 m per month on the piedmont glacier lobes, to several hundred meters per year on faster flowing ice of the alpine terrain. Strain rates calculated from the surface velocity fields are on the order of 10^{-9} s^{-1}. The axes of maximum shortening strain rate are oriented subparallel to the traces of crevasses, indicating that fracturing propagates in the direction of the maximum horizontal compressive stress, as predicted by fracture mechanics theory.

Alpine glaciers that flow through narrow valleys provide the opportunity to investigate the response of the ice to underlying rock structure, where the location of faults and folds can be traced beneath the glacier from geological mapping of the surrounding terrain. In the study area, icefalls are located where the glaciers flow across thrust faults and juxtapose rocks of variable resistance to erosion, and where stair step like topography develops by plucking of rocks on the gently dipping back limb of a large fault propagation fold. The ice fall where the Dome Pass and Chaix Hills thrust faults

pass beneath the Lower Seward Glacier develops by cliff face collapse and retreat as the glacier preferentially plucks rocks from the weaker strata that lie beneath the more indurate and metamorphosed rocks of the Yakutat Group. On the other hand, preferential plucking of gently dipping bedding in the back limb of a fault propagation fold creates the icefall on the Agassiz Glacier where it exits the Chaix Hills in the hanging wall of the Malaspina Fault. In this latter example, the bedding dips gently up glacier, and plucking presumably results in a stair case geometry within the bedrock that forms a topographic step and icefall on the surface of the glacier. This step (cliff face) trend (gently up glacier dipping bedrock surface) geometry is a common geomorphic feature observed in the floors of alpine glacier valleys following retreat of the ice (Hooke, 1991).

The upper section of the Lower Seward Glacier and the central part of the Agassiz Glacier both flow parallel to thrust faults, and in these regions, the highest velocities are located over the trace of the fault surface at the base of the glacier. We propose that this phenomenon is caused by development of water saturated till at the base of the glacier by excavation of the weak and highly fractured and fault rock. That is, linear regions of high surface velocity corresponds to a weak basal layer of till that is sandwiched between the ice and underlying intact bedrock within the fault zone .

The structure of the Seward Glacier Basin and the pattern of ice motion in the Upper Seward Glacier reflects splay faulting at the northwestern end of the Fairweather Fault. The fault that has formed in the dilatational lobe of the strike slip fault tip is a large normal fault that subdivides the basin into western and eastern regions, and diverts westward flowing ice to the south and into the head of the Lower Seward Glacier. Conversely, the Cascade Glacier fault is located within the compressional lobe of the

strike slip fault tip, and if reactivated, will tend to close the head of the outlet valley of the Upper Seward Glacier, while at the same time provide highly fractured rock and weak 'till' to the base of the glacier that will enhance the rate of flow down slope, and tend to widen the valley by erosion.

The dextral offset of 1-2 km at the mouth of the Lower Seward Glacier debauches onto the piedmont and is caused by strike slip motion on the Esker Creek Fault. This fault is therefore accommodating some of the dextral motion along the plate boundary at the expense of motion on the Fairweather transform fault.

Oily Lake occupies a narrow basin formed by erosion at the intersection of the Esker Creek and Malaspina thrust faults. The lake extends beneath the ice and discharges from time to time through englacial or subglacial drainage (s) that are marked by a linear belt of collapse pits on the surface of the ice. Collapse pits can be traced towards Yana Stream, a discharge site at the terminus of the Malaspina Glacier. The subglacier extent of the lake is revealed by the radial crevasses that surround the lake, and movement of the ice towards the lake basin that is revealed by feature tracking.

REFERENCES

Aydin, A., and Nur, A., 1982, Evolution of pull-apart basins and their scale independence: Tectonics, v. 1, p. 91-105.

Ayoub, F., Leprince, S., and Avouac, J.P., 2009, Co-registration and correlation of aerial photographs for ground deformation measurements: ISPRS Journal of Photogrammetry and Remote Sensing, v. 64, p. 551-560.

Allen, C.R., Kamb, W.B., Meier, M.F., and Sharp, R.P., 1960, Structure of the Lower Blue Glacier, Washington: The Journal of Geology, v. 68, no. 6, p. 601-625.

Boulton, G.S. and Hindmarsh, R.C.A, 1987, Sediment Deformation beneath Glaciers: Rheology and Geological consequences: Journal of Geophysical Research , v. 92, no. B9, p. 9050-9082.

Bruhn, R.L., and Haeussler, P.J., 2006, Deformation driven by subduction and microplate collision: Geodynamics of Cook Inlet Basin, Alaska. Geological Society of America Bulletin, v. 118, p. 289-303.

Bruhn, R.L., Forster, R.R., Ford A.L.J., Pavlis, T.L., Vorkink, M., 2010, Structural geology and glacier dynamics, Bering and Stellar Glaciers, Alaska: The Geological Society of America special paper 462, p. 217-233.

Bruhn, R.L., Pavlis, T.L., Plafker, G., and Serpa, L., 2004, Deformation during terrane accretion in the Saint Elias orogen, Alaska: Geological Society of America Bulletin, v. 116, p. 771 -787.

Bruns, T.R., 1983, Model for the origin of the Yakutat block, an accreting terrane in the northern Gulf of Alaska: Geology, v. 11, p. 718-721.

Burgess, E.W., Forster, R.R., Hall, D.K., 2010, Regional Observations of Alaska Glacier Dynamics: American Geophysical Union, Fall Meeting 2010, abstract C23A-0582.

Capps, D.M., Rabus, B., Clague, J.J., and Shugar, D.H., 2010, Identification and characterization of alpine subglacial lakes using interferometric synthetic aperture radar (InSAR): Brady Glacier, Alaska, USA: Journal of Glaciology, v. 56, no. 199, p. 861-870.

Cardozo, N., and Allmendinger, R.W., 2009, SSPX: A program to compute strain from displacement/velocity data: Computers & Geosciences, v. 35, p. 1343-135.

Chapman, J.B., Pavlis, T.L., Gulick, S., Berger, A., Lowe, L., Spotila, J., Bruhn, R.L., Vorkink, M., Koons, P., Barker, A., Picornell, C., Ridgway, K., Hallet, B., Jaeger, J., and McCalpin, J., 2008, Neotectonics of the Yakutat collision: Active Tectonics and Seismic Potential of Alaska: American Geophysical Union, Geophysical Monograph, 179, p. 65-82.

Christeson, G.L., Gulick, S.P.S., Van Avendonk, H.J.A.,Worthington, L., Reece, R.S., and Pavlis, T.L., 2010, The Yakutat terrane: Dramatic change in crustal thickness across the Transition fault, Alaska: Geology, v. 38, no. 10, p. 895-898.

Conway H., Smith B., Vaswani P., Matsuoka K., Rignot E., and Claus P., 2009, A low-frequency ice-penetrating radar system adapted for use from an airplane: Test results from Bering and Malaspina Glaciers, Alaska, USA: Annals of Glaciology, v. 50, p. 93–97.

Doser, D.I., and Lomas, R., 2000, The transition from strike-slip to oblique subduction in southeastern Alaska from seismological studies: Tectonophysics, v. 316, p. 45-65.

Doser, D.I., and Rodriguez, H., 2010, A seismotectonic study of the Southeastern Alaska Region: Tectonophysics, v. 497, no. 1-4, p.105-113.

Doser, D.I., Pelton, J.R., and Veilleux, A.M., 1997, Earthquakes in the Pamplona zone, Yakutat block, south central Alaska: Journal of Geophysical Research, v. 102, p. 24,499-24,511.

Elliott, J.L., Larsen, C.F., Freymueller, J.T., and Motyka, R.J., 2010, Tectonic block motion and glacial isostatic adjustment in southeast Alaska and adjacent Canada constrained by GPS measurements: Journal of Geophysical Research, v. 115, p. 21.

Enkelmann, E., Zeitler, P.K., Pavlis, T.L., Garver, J.I., and Ridgway, K.D., 2009, Intense localized rock uplift and erosion in the St Elias orogen of Alaska: Nature Geoscience, v. 2, p. 360-363.

Estabrook, C.H., Nabelek, J.L., and Lerner-Lam, J.L., 1992, Tectonic model of the Pacific-North American plate boundary in the Gulf of Alaska from broadband analysis for the 1979 St. Elias, Alaska, earthquake and its aftershocks: Journal of Geophysical Research, v. 97, p. 6587–6612.

Eyles, C.H., and Lagoe, M.B., 1990, Sedimentation patterns and facies geometries on a temperate glacially-influenced continental shelf: the Yakataga Formation, Middleton Island, Alaska: Geological Society Special Publication, v. 53, p. 363-386.

Eyles, C.H., Eyles, N., and Lagoe, M.N., 1991, The Yakataga Formation: A late Miocene to Pleistocene record of temperate glacial marine sedimentation: Geological Society of America Special Paper, v. 261, p. 159–187.

Fletcher, H.J., and Freymueller, J.T., 1999, New GPS constraints on the motion of the Yakutat Block: Geophysical Research Letters, v. 26, p. 3029-3032.

Fletcher, R.C., and Pollard, D.D., 1981, Anticrack model for pressure solution surfaces: Geology, v. 9, p. 419-424.

Ford, A.L., Forster, R.R., and Bruhn, R.L., 2003, Ice Surface velocity patterns on Seward Glacier, Alaska/Yukon, and their implications for regional tectonics in the Saint Elias Mountians: Annals of Glaciology, v. 36, p. 21-28.

Fountain, A.G., and Walder, J.S., 1998, Water through temperate glaciers: Reviews in Geophysics, v. 2, no. 3, p. 299-328.

Fowler, A. C., 1982, Waves on glaciers: Journal of Fluid Mechanics, v. 120, p. 283–321.

Gerbi, C., 2003, Kitchen table rheology, play dough and flubber flow laws, http://www.geology.um.maine.edu/geodynamics/AnalogWebsite/Projects2003/Gerbi_2003/index.html.

Gudmundsson G., 2003, Transmission of basal variability to a glacier surface: Journal of Geophysical Research, v. 108, p. 19.

Gustavson, T.C., and Boothroyd, J.C., 1987, A depositional model for outwash, sediment sources, and hydrologic characteristics, Malaspina Glacier, Alaska: A modern analog of the southeastern margin of the Laurentide Ice Sheet: Geological Society of America Bulletin, v. 99, p. 187-200.

Hallet, B., Hunter, L., and Bogen, J., 1996, Rates of erosion and sediment evacuation by glaciers: A review of field data and their implications: Global Planetary Change, v. 12, p. 213-235.

Harper, J.T., Humphrey, N.F., and Pfeffer, W.T., 1998, Crevasse Patterns and the strain rate tensor: a high resolution comparison: Journal of Glaciology, v. 44, no. 146, p. 68-76.

Hooke, R.L., 1991, Positive feedbacks associated with erosion of glacial cirques and over deepenings: Geological Society of America Bulletin, v. 103, no. 8, p. 1104-1108.

Hubbert, M.K., 1937, Theory of scale models as applied to the study of geologic structures, v. 38, no. 10, p. 1459-1519.

Jensen, J.R., 2005, Introductory Digital Image Processing: Prentice Hall, 3rd edition, 525 pp.

King, C.A.M., and Lewis, W.V., 1961, A tentative theory of ogive formation: Journal of Glaciology, v. 3, no. 29, p. 913-939.

Krimmel, R.M., and Meier, M.F., 1975, Glacier applications of ERTS images: Journal of Glaciology, v. 15, p. 391–402.

Leprince, S., Ayoub, F., Klingert, Y., and Avouac, J.P., 2007a, Co-Registration of Optically Sensed Images and Correlation (COSI-Corr): an operational methodology for ground deformation measurements: Geoscience and Remote Sensing Symposium.

Leprince, S., Barbot, S., Ayoub, F., and Avouac, J.P., 2007b, Automatic and Precise Orthorectification, Coregistration, and Subpixel Correlation of Satellite Images, Application to Ground Deformation Measurements: Geoscience and Remote Sensing, IEEE Transactions, v. 45, p. 1529-1558.

Lingle, C.S. and Fatland, D.R., 2003, Does englacial water storage drive temperate glacier surges?: Annuals of Glaciology, v. 36, p. 14–20.

Lingle, C.S., Fatland, D.R., Voronina, V., Ahlna¨s, K., and Troshina, E., 1997, Dynamic behaviour of the Bering Glacier–Bagley Ice Field system during a surge, and other measurements of Alaskan glaciers with ERS imagery: Third ERS Scientific Symposium Proceedings, p. 995–1000.

Meigs, A. and Sauber, J., 2000, Southern Alaska as an example of the long-term consequences of mountain building under the influence of glaciers: Quaternary Science Reviews, v. 19, p. 1543-1562.

Molnia, B.F., 2001, Glaciers of Alaska: Alaska Geography, v. 28.

Molnia, B.F., and Jones, J.E., 1989, View through ice: Are unusual airborne radar backscatter features from the surface of the Malaspina glacier, Alaska. Expressions of subglacial morphology?: Eos Transaction. AGU 70, p. 701-701.

Muskett, R.R., Lingle, C.S., Tangborn, W.V., and Rabus, B.., 2003, Multi-decadal elevation changes on Bagley Ice Valley and Malaspina Glacier: Alaska. Geophysical Research Letters, v. 30, p. 1857.

Muskett, R.R., Lingle, C.S., Sauber, J.M., Post, A.S., Tangborn, W.V., Rabus, B.T., 2008, Surging, accelerating surface lowering and volume reduction of the Malaspina Glacier system, Alaska, USA, and Yukon, Canada, from 1972 to 2006: Journal of Glaciology, v. 54, no. 188, p. 788-800.

Page, R.A., Stephens, C.D., and Lahr, J.C., 1989, Seismicity of the Wrangell and Aleutian Wadati-Benioff zones and the North American plate along the Trans-Alaska Crustal Transect, Chugach Mountains and Copper River basin, southern Alaska: Journal of Geophysical Research, v. 94, p. 16,059–16,082.

Pavlis, T.L., Picornell, C., Serpa, L., Bruhn, R.L., and Plafker, G., 2004, Tectonic processes during oblique collision: Insights from the St. Elias orogen, northern North American Cordillera: Tectonics, v. 23, p. 14.

Plafker, G., 1987, Regional geology and petroleum potential of the northern Gulf of Alaska continental margin: Earth Science Series, v. 6, p. 229–268.

Plafker, G., and Thatcher, W., 2008, Geological and geophysical evaluation of the mechanisms of the great 1899 Yakutat Bay earthquakes: Active Tectonics and Seismic Potential of Alaska, Geophysical Monograph Series, v. 179.

Plafker, G., Bruns, T.R., and Page, R.A., 1975, Interim report on petroleum resource potential and geologic hazards in the Outer Continental Shelf of the Gulf of Alaska Tertiary Province: U.S. Geological Survey Open-File Report 75-592, p 74.

Plafker, G., Gilpin, L.M., and Lahr, J.C., 1994a, Neotectonic map of Alaska: Geology of North America, v. G-1, scale 1:2,500,000, 1 sheet.

Plafker, G., Hudson, T., Bruns, T.R., and Rubin, M., 1978, Late Quaternary offsets along the Fairweather Fault and crustal plate interactions in southern Alaska: Canadian Journal of Earth Sciences, v. 15, p. 805-816.

Plafker, G., Moore, J.C., and Winkler, G.R., 1994b, Geology of the southern Alaska margin: Geology of North America, v. G-1, p. 389-449.

Post, A., 1969, Distribution of surging glaciers in western North America: Journal of Glaciology, v. 8, p. 229–240.

Richter, D.H., Preller, C.C., Labay, K.A., and Shew, N.B., 2006, Geologic Map of the Wrangell-Saint Elias National Park and Preserve, Alaska: U.S. Geological Survey Scientific Investigations, Map 2877.

Sauber, J., Molnia, B., Carabajal, C., Luthcke, S., and Muskett, R., 2005, Ice elevations and surface change on the Malaspina Glacier: Alaskan Geophysical Research Letters, v. 32.

Sauber, J., Plafker, G., Molnia, B.F., and Bryant, M.A., 2000, Crustal deformation associated with glacial fluctuations in the eastern Chugach Mountains, Alaska: Journal of Geophysical Research, v. 105, p. 8055–8077.

Scherler, D., Leprince, S., and Strecker, M.R., 2008, Glacier-surface velocities in alpine terrain from optical satellite imagery--Accuracy improvement and quality assessment: Remote Sensing of Environment, v. 112, p. 3806-3819.

Sharp, R.P., 1951, Accumulation and ablation on the Seward-Malapsina Glacier System, Canada-Alaska: Geological Society of America Bulletin, v. 62, p.725-744.

Sharp, R.P., 1958, Malaspina Glacier, Alaska: Geologic Society of America Bulletin, v. 69, p. 617–646.

Shekarforoush, H., Berthod, M., and Zerubia, J., 1996, Subpixel image registration by estimating the polyphase decomposition of cross power spectrum: Computer Vision and Pattern Recognition, IEEE Computer Society Press, pp. 532–537.

Shennan, I., Bruhn, R., and Plafker, G., 2009, Multi-segment earthquakes and tsunami potential of the Aleutian megathrust: Quaternary Science Reviews, v. 28, p. 7-13.

Spotila, J.A., Buscher, J.T., Meigs, A.J., and Reiners, P.W., 2004, Long-term glacial erosion of active mountain belts: Example of the Chugach–St. Elias Range, Alaska: Geology, v. 32, p. 501 -504.

Tarr, R.S., and Martin, L., 1912, The earthquakes of Yakutat Bay, Alaska in September 1899: U.S. Geological Survey Professional Paper, v. 69, p.135.

Winther, J., 1993, Landsat TM derived and in situ summer reflectance of glacier in Svalbard: Polar Research, v. 12, p. 37-55.

Worthington, L.L, Guilck, S.P.S., and Pavlis, T.L., 2010, Coupled stratigraphic and structural evolution of a glaciated orogenic wedge, offshore St. Elias orogen, Alaska: Tectonics, v. 29,

Zeng, Q., Cao, M., Feng, X., Liang, F., Chen, X., and Sheng, W., 1984: A study of spectral reflection characteristics for snow, ice and water in the north of China: Hydrological Applications of Remote Sensing and Remote Data Transmission, Proceedings of the Hamburg Symposium, v. 145, p. 451-462.